UNIVERSITATEA BABEŞ-BOLYAI
BABEŞ-BOLYAI TUDOMÁNYEGYETEM
BABEŞ-BOLYAI UNIVERSITÄT
BABEŞ-BOLYAI UNIVERSITY
TRADITIO ET EXCELLENTIA

DEVELOPMENT OF SMART MATERIALS FOR HOMOJUNCTION ORGANIC SOLAR CELLS, ELECTRODE MATERIALS AND PHOTOLUMINESCENT CARBON DOTs

PhD Thesis in Chemistry

by

Daniel-Florin BOGOȘEL

BABEŞ-BOLYAI UNIVERSITY
Faculty of Chemistry and Chemical Engineering

Scientific Advisor:

Prof. Dr. Ion GROSU

Cluj-Napoca, 2025

UNIVERSITATEA BABEŞ-BOLYAI
BABEŞ-BOLYAI TUDOMÁNYEGYETEM
BABEŞ-BOLYAI UNIVERSITÄT
BABEŞ-BOLYAI UNIVERSITY
TRADITIO ET EXCELLENTIA

DEVELOPMENT OF SMART MATERIALS FOR HOMOJUNCTION ORGANIC SOLAR CELLS, ELECTRODE MATERIALS AND PHOTOLUMINESCENT CARBON DOTs

PhD student

Daniel-Florin BOGOȘEL

Public defence: 11th September 2025

Thesis Committee:

President:	*Assoc. Prof. Dr. Richard-Attila Varga*	*Babeş-Bolyai University, Cluj-Napoca*
Scientific advisor:	*Prof. Dr. Ion Grosu (C.M. of the Romanian Academy)*	*Babeş-Bolyai University, Cluj-Napoca*
Reviewers:	*Prof. Dr. Habil. Ing Monica-Ioana Toşa*	*Babeş-Bolyai University, Cluj-Napoca*
	Dr. Monica Lucia Veca (Senior Researcher- CS I)	*National Institute for Research and Development in Microtechnologies, IMT Bucharest*
	Assoc. Prof. Dr. Ing Lorant Andras Szolga	*Technical University of Cluj-Napoca*

Cluj-Napoca, 2025

Abbreviations and symbols:

OPV	Organic Photovoltaic
D-A	Donor-Acceptor
HOSCs	Homojunction Organic Solar Cells
PCE	Power Conversion Efficiency
J_{SC}	Short Circuit Current
V_{OC}	Open Circuit Voltage
SMOSCs	Single-Material Organic Solar Cells
D	Donor
A	Acceptor
UV-vis	Ultraviolet-visible
NMR	Nuclear Magnetic Resonance
CV	Cyclic Voltammetry
OSC	Organic Solar Cells
COF	Covalent Organic Framework
CCOF	Cationic Covalent Organic Framework
SEM	Scanning Electron Microscopy
DSC	Differential Scanning Calorimetry
TGA	Thermogravimetric Analysis
FTIR	Fourier-Transform Infrared Spectroscopy
XRD	X-ray Diffraction Spectroscopy
XPS	X-ray Photoelectron Spectroscopy
MS	Mass Spectrometry
CDs	Carbon Dots
CIE	Commission Internationale de l'Eclairage (International Commission on Illumination)
LED	Light-Emitting Diode
OLED	Organic Light-Emitting Diode
CRI	Colour Rendering Index
rGOs	Reduced Graphene Oxides

Contents

General Introduction 5

Chapter 1: Organic Materials for Homojunction Organic Solar Cells **7**

1.1 Introduction 7

1.2 Results 8

1.2.1 Optical Properties 9

1.2.3 Electrochemical Properties 10

1.2.2 Evaluation of the Photovoltaic Properties 11

1.3 Conclusions 11

Chapter 2: Cationic Covalent Organic Frameworks **13**

2.1 Introduction 13

2.2 Results 14

2.2.1 Synthesis of New Cationic COFs 14

2.2.2 Characterisation of New Cationic COF.Cat.1 17

2.2.3 Characterisation of the New Cationic COF.Cat.2 19

2.3 Conclusions 22

Chapter 3: Anion exchange membranes with potential applications in Zinc-air batteries **23**

3.1 Introduction 23

3.2 Results 23

3.2.1 Synthesis of Anion Exchange Membranes 23

3.2.2 Characterisation of Anion Exchange Membranes 27

3.3 Conclusions 30

Chapter 4: *Contributions to Carbon Dots Materials in Photovoltaics* **31**

4.1 Introduction 31

4.2 Results and Discussions 32

4.2.1 Morphological Properties of CDs-PDA 33

4.2.2 Photoluminescent Properties of CDs 34

4.2.3 Investigation of transport properties for CDs-PDA and CDs-NIPAM materials 36

4.2.4 CDs-graphene hybrids with broad photoresponsivity 38

4.3 Conclusions 40

Chapter 5: Access to Unsymmetrical Macrocycles for Surface Deposition **41**

5.1 Introduction 41

5.2 Results and Discussion 41

5.2.1 Synthesis and characterisation of unsymmetrical macrocycle 42

5.2.2 Synthesis and structural characterisation of Macro-Tpy derivative 45

5.2.3 Synthesis and characterisation of a tripodal anchor 46

5.3 Conclusions 51

General Conclusions 52

General Introduction

The thesis is structured into five chapters concerning new: a) materials for Homojunction Organic Solar Cells; b) cationic Covalent Organic Frameworks; c) anion exchange membranes; d) electroluminescent carbon dots; e) unsymmetric macrocycle and tripodal anchor for graphene deposition.

Chapter one explores the absorption properties, electrochemical behaviour, and photovoltaic performance of eight newly synthesised D-π-A type compounds. These structures feature triarylamine and its derivatives as electron-donating groups, thiophene-based moieties as π-conjugated linkers, and 2-(3-oxo-2,3-dihydro-1H-inden-1-ylidene-1-ylidene) malononitrile as the electron-acceptor fragment. The compounds were evaluated for their applicability in homojunction organic solar cells, compatible with both conventional and inverted architectures.

Chapter two outlines the synthesis of two novel Cationic Covalent Organic Frameworks (COFs) intended for hydrogel applications in zinc–air batteries. Engineered for stability under alkaline conditions, these cationic COFs were characterised using FT-IR, TGA, DSC, XRD, and SEM techniques.

Chapter three presents the synthesis and characterisation of nine novel anion exchange membranes designed for use in zinc–air batteries. The synthetic pathway involves a three-step reaction sequence starting from commercially available precursors. Experimental results reveal that targeted modifications of the reactants enhanced the physicochemical properties of the membranes. Characterisation was performed using FT-IR, DSC, TGA, and SEM techniques.

Chapter four describes the synthesis of five carbon dot materials via simple surface passivation of carbon nanopowder using 1,4-phenylenediamine and four polymers: Poly(ethylene glycol) bis(3-aminopropyl) amine-terminated (PEG1500N), Poly(propylene glycol) bis(2-aminopropyl ether) (Jeffamine D2000), Poly(N-isopropyl acrylamide) amine-terminated (NIPAM2000), and Poly(N-isopropyl acrylamide) N-hydroxysuccinimide ester-terminated (PNIPAM-NHS2000). The electroluminescent properties of carbon dots passivated with PDA and NIPAM were evaluated in a multilayer light-emitting diode, where the carbon dots served as the active layer. Additionally, carbon dots modified with

NIPAM and PEG were integrated with N-doped graphene oxide to fabricate flexible photodetectors, with potential application in real-time health monitoring medical devices.

The final chapter describes the synthesis of a novel unsymmetrical macrocycle engineered for conjugation with a terpyridine derivative and a tripodal anchoring unit. The synthetic strategies for assembling the Macro-Tpy conjugate and the tripodal anchor are detailed, and their molecular architectures were elucidated using NMR spectroscopy and mass spectrometry.

Chapter 1: Organic Materials for Homojunction Organic Solar Cells

1.1 Introduction

Over the years, researchers have been interested in simplifying the synthesis of organic materials and hence OPVs. These simplifications have significantly advanced the development of single-material organic solar cells (SMOSCs) for OPV applications. From SMOSCs containing polymers to those employing triads and dyads as active materials, the most streamlined versions are based on small π-conjugated molecules (HOSCs). These SMOSCs are based on ambivalent materials that integrate covalently bonded electron donor (D) and electron-acceptor (A) groups (**Figure 1**), which enable fundamental functions such as light absorption, exciton dissociation and charge transport.[1,2]

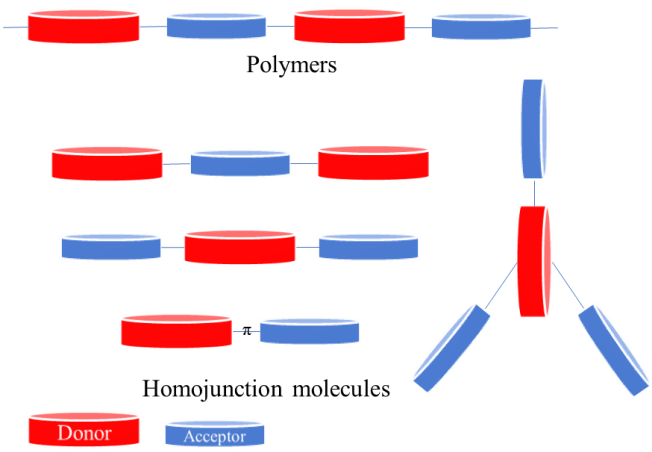

Figure 1: Schematic diagram for homojunction models

The operating principle of organic solar cells under sunlight can be described in four steps (**Figure 2**):

1) The generation of excitons (electron-hole pair) happens after the photon is absorbed by the material.

2) Exciton diffusion to the D/A interface.

[1] J. Roncali and I. Grosu, *Adv. Sci.* **2019**, *6*, 1801026
[2] J. Roncali, *Adv. Energy Mater.* **2011**, *1*, 147

3) Exciton dissociation into free charges at the D/A interface results in an electron transfer from the LUMO of the D to the LUMO of the A and finally charge transport.

4) Charge collection at the two electrodes to generate the photocurrent.

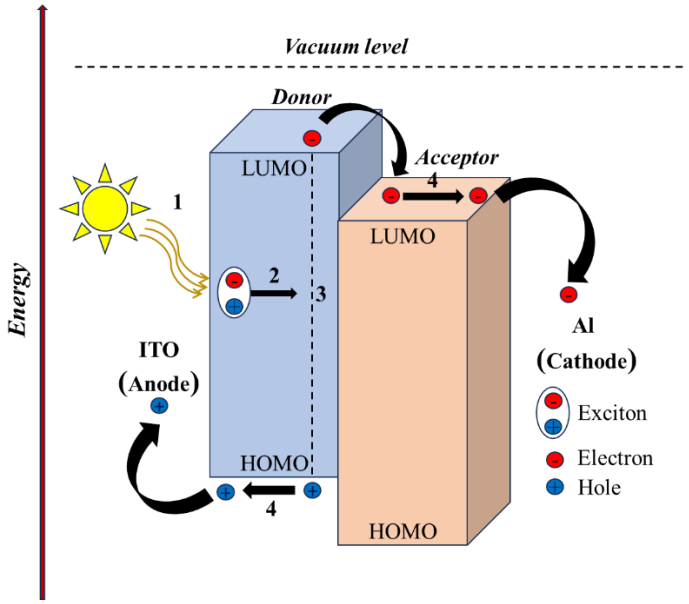

Figure 2: Schematic illustration of **the** photovoltaic conversion mechanism in OSCs

1.2 Results

This research aims to develop new D-π-A materials using triphenylamine (TPA) and its derivatives as electron-donating groups and 2-(3-oxo-2,3-dihydro-1H-inden-1-ylidene-1-ylidene) malononitrile as electron acceptor unit, covalently linked via a π-spacer constructed from different thiophen derivatives. These types of compounds (compounds **1-8**, **Figure 3**) are straightforward to synthesise and exhibit properties that enable their implementation into devices *via* the solution-based spin coating method.

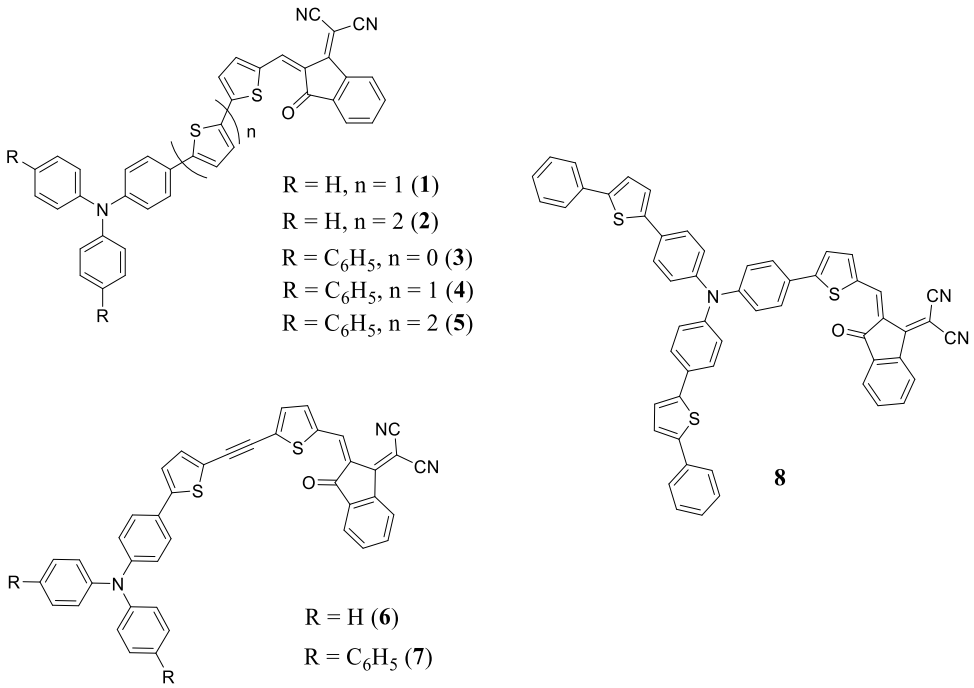

Figure 3: Chemical structures of the target D-π-A (**1-8**) molecules

Eight new molecules D-π-A (**Figure 3**) have been designed and synthesised. These molecules feature the TPA donor block as well as its derivatives enriched with phenyl and 2-phenyl thiophene residues, aimed at enhancing donor capacity and further improving efficiency. For the π-spacer, thiophene, bithiophene, terthiophene and a 1,2-di(thiophen-2-yl) ethyne group were used to investigate how increasing the spacer length and introducing a triple bond between two thiophenes affects the molecular properties, particularly through enhanced π-conjugation and the connection between the D and A moieties. For all compounds, the same well-known acceptor derivative (2-(3-oxo-2,3-dihydro-1H-inden-1-ylidene-1-ylidene) malononitrile) was employed.

1.2.1 Optical Properties

The spectroscopic analyses of the target compounds were carried out in methylene chloride solutions and thin films spin-cast on glass from chloroform or chloroform/1,1,2,2-tetrachloroethane solutions. The UV-vis spectra of all compounds show two bands between 300-450 nm ascribed to the π-π^* transition of the triarylamine donor moiety and a more intense transition band between 580-620 nm (visible area) assigned to an internal charge transfer (ICT) from the donor to the acceptor unit. Further information about the λ_{max} in

solution and films, optical bandgap data (E_g^{opt}), estimated from the long-wavelength absorption edge of thin films, is also summarised in **Table 1**

Table 1. UV-vis absorption data ([s:] CH_2Cl_2 solutions; [f:] thin films spun-cast on glass) and electrochemical data (0.10 M Bu_4NPF_6/CH_2Cl_2, Pt electrodes, ref SCE, scan rate = 100 mV s^{-1}) for compounds **1-8** and reference **C**:

Compd	λ_{max}^{s} [nm]	ε_{max} [$M^{-1}cm^{-1}$]	λ_{max}^{f} [nm]	E_g^{opt} [eV][a]	E_{pa}^{1}, E_{pa}^{2} [V]	E_{pc} [V]	E_{HOMO} [eV][b]	E_{LUMO} [eV][b]	E_g [eV][c]
C	603	52000	625	1.65	1.00	-0.79	-5.55	-4.04	1.51
1	610	51700	625	1.55	0.87; 1.28	-0.79	-5.43	-4.04	1.39
2	615	47900	640	1.47	0.81; 1.1	-0.75	-5.38	-4.06	1.32
3	613	59500	645	1.62	0.97	-0.75	-5.53	-4.04	1.49
4	613	53400	645	1.53	0.85; 1.28	-0.77	-5.4	-4.05	1.35
5	608	43200	635	1.52	0.8; 1.08	-0.75	-5.36	-4.06	1.30
6	612	44800	610	1.61	0.92	-0.80	-5.49	-4.00	1.49
7	580	36900	620	1.63	0.88	-0.67	-5.45	-4.12	1.33
8	620	47400	655	1.59	0.86; 1.26	-0.86	-5.43	-4.01	1.42

[s:] CH_2Cl_2 solutions; [f:] films; [a:] estimated from the long-wavelength absorption onset of thin films; [b:] estimated from the onset of the oxidation and reduction processes; [c:] band gap calculated from the difference between HOMO-LUMO levels

1.2.3 Electrochemical Properties

The electrochemical properties of the compounds have been analysed by cyclic voltammetry (CV) in methylene chloride, using 0.1M of tetrabutylammonium hexafluorophosphate as a supporting electrolyte and a scan rate of 100 mVs^{-1}. The redox properties revealed that these TPA-based materials undergo one or two chemically reversible oxidation peaks and one chemically irreversible reduction wave. The CV results show that the HOMO which controls the HOMO-LUMO gap is determined by the TPA, and π-conjugated connector and the lowest unoccupied molecular orbital (LUMO) is controlled by the acceptor unit. The electrochemical gap values (E_g) determined by the difference of HOMO and LUMO levels estimated from the onset of the first oxidation and reduction waves are consistent with the optical band gap values observed by UV-vis spectroscopy.

1.2.2 Evaluation of the Photovoltaic Properties

The photovoltaic properties of compounds **1-8** have been investigated on direct and inverted homojunction cells of 28 mm^2 active area of structure ITO/MoO_3/**M**/Bphen/Aluminium and ITO/ZnO/**M**/MoO_3/Aluminium where **M** is the active material (ca. 25 nm thick film), fabricated by spin-coating method from chloroform for compounds **3**, **5** and **6**, 1,1,2,2-tetrachloroethane (TCE) for compounds **8** and a mixture of chloroform: TCE (1:1) for compounds **1**, **2** and **4**. The vacuum deposition method was also used, but the results were always negative for all compounds, and no films were obtained. A higher evaporation temperature led to the decomposition of the compounds, and a significant amount of residues was found in the crucible after thermal evaporation under high vacuum. Overall, these compounds were processable *via* the solution technique. The photovoltaic characteristics of HOSCs based on D-π-A systems are summarised in **Table 2**; the best *PCE* values in inverted cells were highlighted in red for the compounds studied.

Table 2. Photovoltaic characteristics of SMOSCs based on **1-8** under AM 1.5 simulated solar light with a power light intensity of 100 mW cm^{-2} (by spin-coating method)

Compd.	V_{oc}[a] *[V]*	J_{sc}[a] *[mA/cm²]*	*FF*[a] *[%]*	*PCE [%]*[b]	
				Inverted	**Direct**
C	1.05	3.49	23.6	**0.86**	*0.46*
1	0.74	1.81	25.7	**0.34**	*0.14*
2	0.73	0.91	26.4	**0.18**	*0.05*
3	1.02	1.81	20.5	**0.38**	*0.16*
4	0.58	1.28	30.5	**0.23**	*0.11*
5	0.66	1.52	26.0	**0.26**	*0.14*
6	0.86	2.05	25.1	***0.44***	*0.15*
7[c]	-	-	-	**-**	-
8	0.90	1.79	28.9	***0.46***	*0.10*

[a] photovoltaic parameter for inverted cells, [b] *PCE* values depend on the type of cell architecture, direct and inverted [c] compound **7** could not be analysed

1.3 Conclusions

Eight new D-π-A type compounds suitable for HOSCs were synthesised, characterised and analysed by investigating their optical and electrochemical properties. Seven of these compounds were also tested for their photovoltaic properties in both direct and inverted cell architectures using the spin-coating method.

The results revealed that the energy conversion efficiencies for compounds **1-6** and **8** were significantly higher in inverted cells compared to direct cells. Changing the π-spacer greatly affects device performance. Replacing the reference π-spacer (from reference **C**) with two or three thiophenes (compounds **2** and **3**) drastically reduces the *Jsc* and *PCE* values, even though an increase in the *FF* is observed.

Tuning the degree of conjugation length by introducing a triple bond between the thiophenes modifies the charge transport pathways beneficially, and this was observed in the *PCE* values of compound **6** (0.44%) and compound **2** (0.18%).

Comparing reference compound **C** and compound **3**, where the donor unit was modified, resulted in more than a 50% reduction in both *Jsc* and *PCE*, while only slightly affecting *Voc*. This suggests that the donor unit plays a crucial role in charge generation and transport, making its optimisation essential for enhancing efficiency.

Compounds **3**, **4** and **5** have the same donor and acceptor units but vary in the length of the π-spacer, which shows that there is no direct relationship between the length of the π-spacer and the PCE values.

Solution processing via the spin-coating method turned out to be the most efficient to obtain functional films. Attempts at vacuum deposition resulted in negative outcomes due to thermal decomposition.

The X-ray analysis of target compound **2** revealed the presence of two crystallographically independent molecules, distinguished by the relative configurations of their three thiophene rings: *syn-syn* in one molecule and *syn-anti* in the other. Comparable arrangements were observed in the X-ray structure of the intermediate aldehyde **24**.

Chapter 2: Cationic Covalent Organic Frameworks

2.1 Introduction

Covalent Organic Frameworks are a new class of porous materials, first invented and reported by Prof. Omar Yaghi and collaborators in 2005. A cyclomerization reaction of 1,4-phenyl diboronic acid and a condensation reaction between 1,4-phenyl diboronic acid and hexahydroxytriphenylene led to two porous crystalline materials with rigid architectures and pore sizes varying from 7 to 27Å, with high thermal stability, high surface areas (711 and 1590 m^2/g) and permanent porosity.[3] Since 2005, interest in COF has grown significantly, and hundreds of COF structures have been reported in the literature.[4,5,6,7]. Depending on the desired properties of the COF, the final structure can be modified by selecting the monomers and the types of bonds, so the structural design can be associated with the Lego™ game (**Figure 2.0)**.

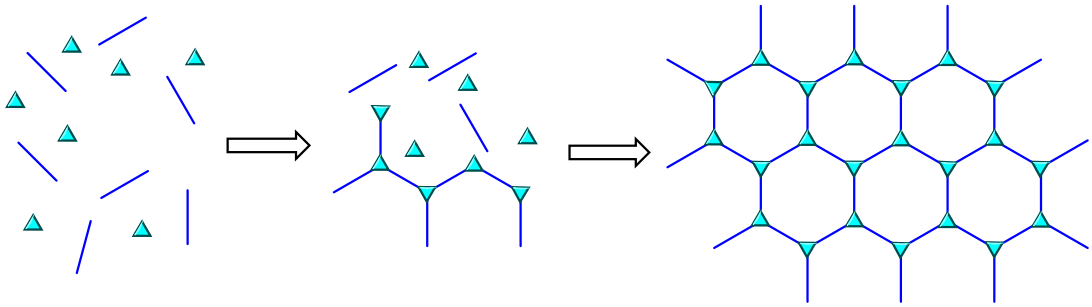

Figure 2.0: Diagram of 2D COF forming from two building blocks

[3] A. P. Cote, A. I. Benin, N. W. Ockwig, M. O'Keeffe, A. J. Matzger, O. M. Yaghi, *Science*, **2005**, *310*, 1166
[4] N. Huang, L. Zhai, D. E. Coupry, M. A. Addicoat, K. Okushita, K. Nishimura, T. Heine, D. Jiang, *Nat. Commun.* **2016**, *7*, 12325
[5] S. P. Teong, Y. Zhang, *Chem. Nano. Mat.* **2023**, *9*, e202300263
[6] Y. Su, B. Li, H. Xu, C. Lu, S. Wang, B. Chen, Z. Wang, W. Wang, K. Otake, S. Kitagawa, L, Huang, C. Gu, *J. Am. Chem. Soc.* **2022**, *144*, 18218
[7] J. Gong, Y. Chen, A. Wenwei, X. Zhang, J. Ma, Z. Xie, P. Li, A. Huang, S. Zhang, Q. Liao, *J. Hazard. Mater.* **2024**, *472*, 134563

2.2 Results

The main objective of this research is to obtain two cationic COFs, **COF.Cat.1** and **COF.Cat.2**, respectively, to characterise them and to study their properties on ZAB, and the behaviour in hydrogels.

2.2.1 Synthesis of New Cationic COFs

To synthesise the cationic **COF.Cat.1**, solvothermal conditions have been applied, combining quaternary amine **1.7** (synthesised previously) with commercially available aldehyde **1.8** in a 3:2 ratio at 120°C for three days. This results in the formation of the cationic COF featuring imine bonds between the amine and aldehyde groups (**Scheme 2.0**).

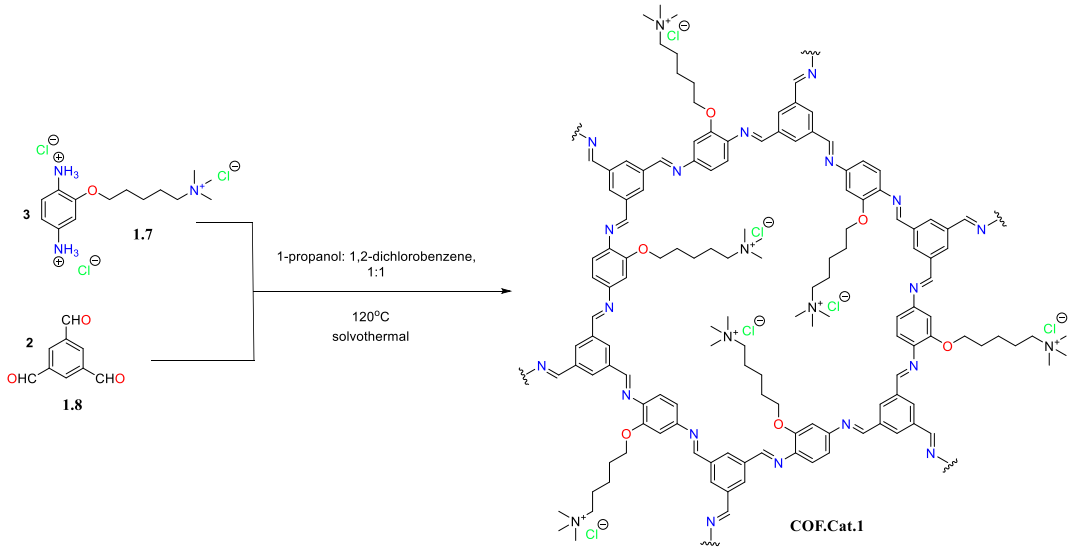

Scheme 2.0: Synthetic strategy for obtaining Cationic **COF.Cat.1**

To see if this cationic COF is stable under basic conditions, a ^{1}H-NMR experiment was conducted and is shown in **Figure 2.**1. The changes in signal intensity in the ^{1}H-NMR spectra suggest that there is a slight hydrolysis or that the set of modifications includes the change of the chloride counter-anion to hydroxyl.

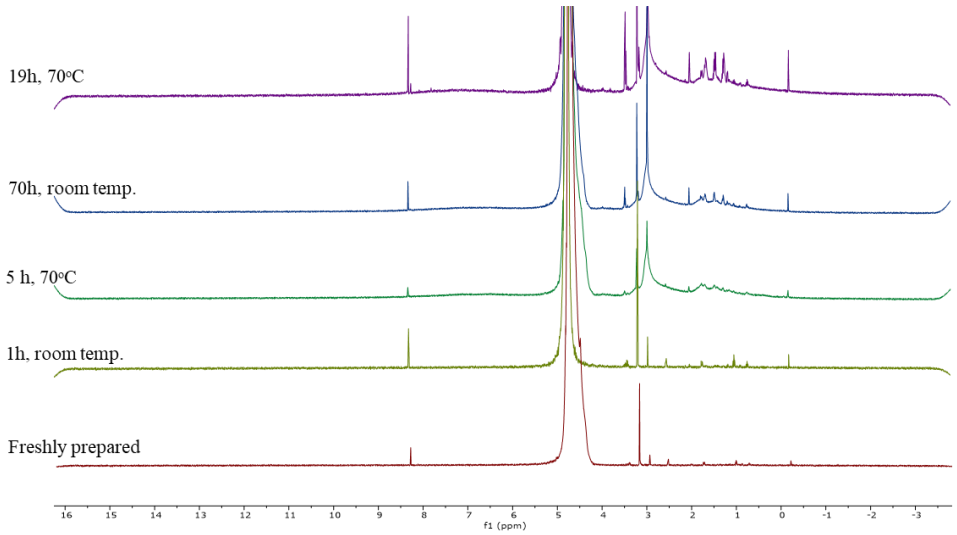

Figure 2.1. ^{1}H-NMR (600 MHz) spectra in 1M sol. NaOD/D_2O

The second cationic COF was much simpler to obtain because it was synthesised using commercially available compounds, 1,4-phenylenediamine and aldehyde **1.8,** using the same ratio between the amine and aldehyde (3:2), but in this case, no solvothermal conditions were used. Thus, by reacting amine **1.1** with aldehyde **1.8** in a mixture of THF: methanol under reflux for three days (**Scheme 2.1**), **COF.2A** containing imine bonds was obtained.

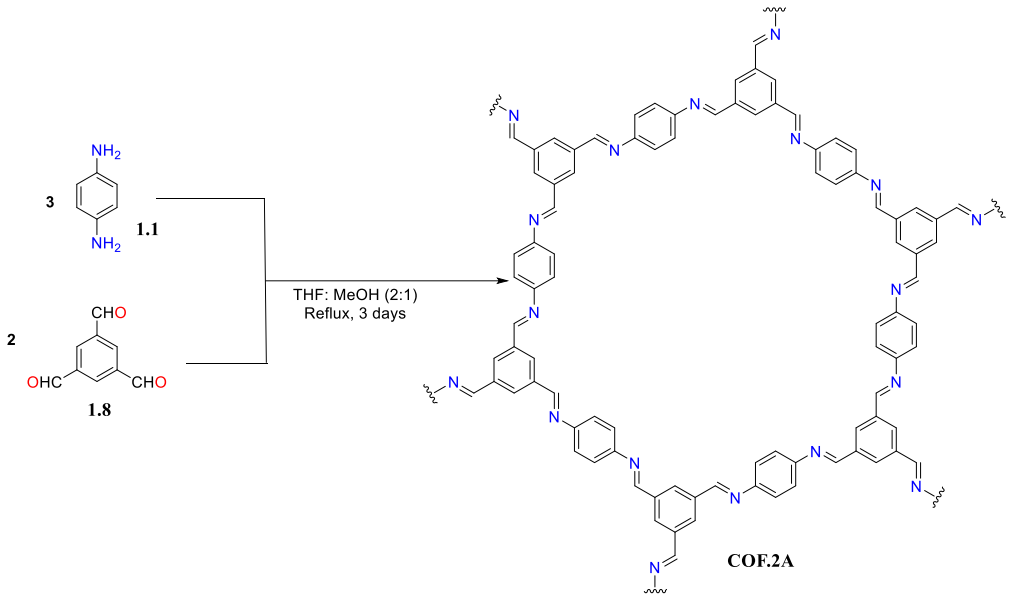

Scheme 2.1: Synthetic strategy for obtaining imine **COF.2A**

Next, the imine **COF.2A** was subjected to a reduction reaction with $NaBH_4$ to stabilise the structure, so the imine was reduced to amine, obtaining **COF.2B,** which was alkylated with methyl iodide to quaternate the amine groups. After this step cationic **COF.Cat.2** was

obtained (**Scheme 2.2**). In this case, the alkylation proceeded using two methods, first a heterogeneous process when the **COF.2B** was suspended in chloroform and stirred at room temperature with a big ratio of methyl iodide, synthesis adapted from the literature,[8] and second, using a Mixer Mill device, **COF.2B** was mixed with an excess of methyl iodide, and grinding for 90 minutes with a frequency of 30 Hz/s.

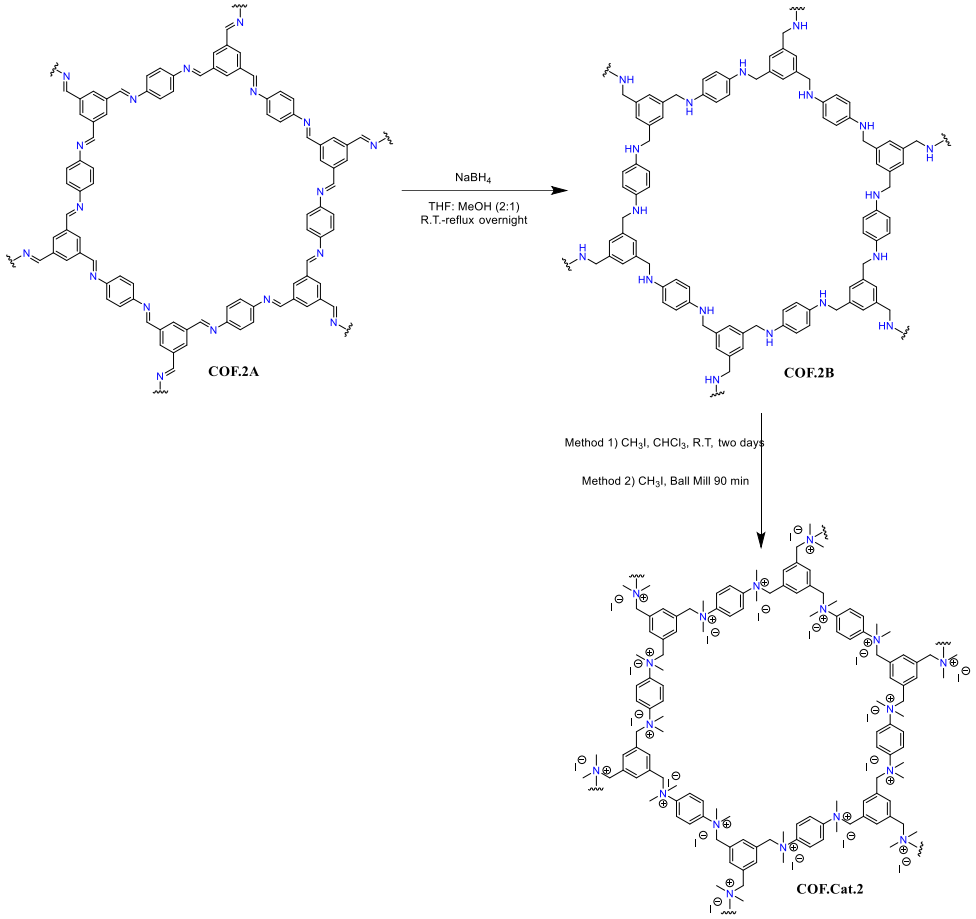

Scheme 2.2: Reducing and alkylation steps for obtaining cationic **COF.Cat.2**

Fourier Transform Infrared Spectroscopy (FTIR), Scanning Electron Microscopy (SEM), Differential Scanning Calorimetry (DSC), and X-ray diffraction spectroscopy (XRD) were used to characterised the cationic COFs.

[8] S.T. Yang, J. Kim, H.Y. Cho, S. Kim, W.S. Ahn, *RSC Adv.* **2012**, *2*, 10179

2.2.2 Characterisation of New Cationic COF.Cat.1

Fourier-Transform Infrared spectroscopy (FTIR) analysis was performed on COF.Cat.1 (**Figure 2.2**). The disappearance of the band is associated with the stretching vibration of C=O from the aromatic amine in the IR spectra of COF.Cat.1 indicates the complete consumption of the aldehyde. Additionally, the absence of bands corresponding to the primary amine salt (compound 1.7) further supports this. The band at 3016 cm-1 is attributed to the stretching vibrations of =C-H from aromatic rings, while the bands at 2943 cm-1 and 2870 cm-1 correspond to the stretching vibrations of -CH_2- from the alkyl chain. Notably, the band observed at 1630 cm-1 corresponds to the stretching vibration of the C=N group, confirming the presence of iminic bonds within the cationic COF molecular structure.

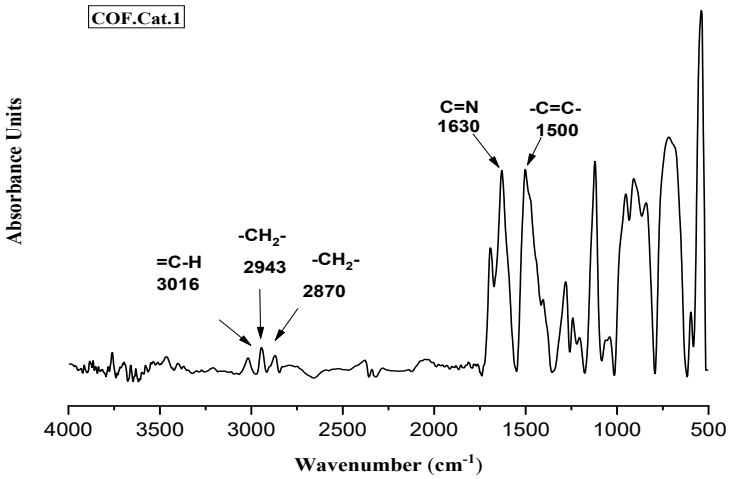

Figure 2.2: FT-IR spectra between 800 and 4000 cm^{-1} of cationic **COF.Cat.1**

X-ray diffraction spectroscopy (XRD) was conducted and showed a single broad peak at 2θ= 21° (**Figure 2.3 A)**, suggesting a low crystallinity and poor π-π stacking between the layers of the structure which can be affected by the charge repulsion between quaternary amines groups and counter-anion, similar behaviour was reported to the

literature.[9,10] But π-π stacking can also be affected by alkyl side chains, resulting in such low crystallinity.

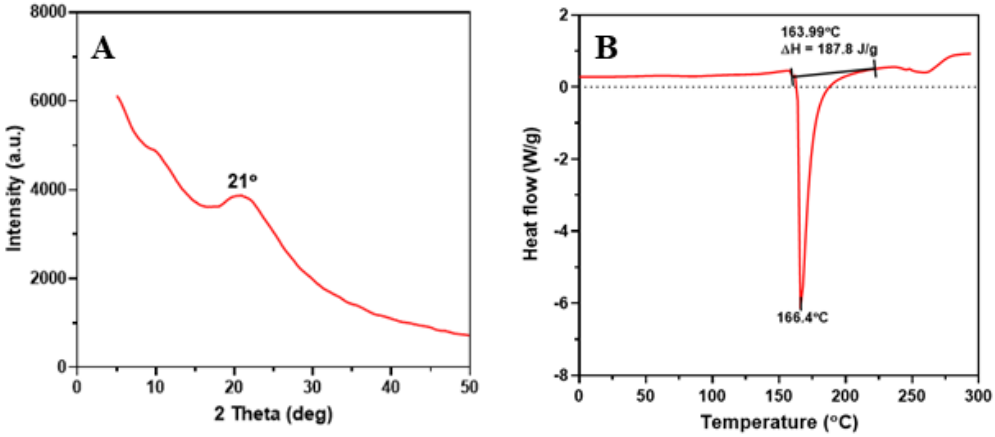

Figure 2.3: **A**) X-ray diffraction pattern, **B**) DSC thermogram of **COF.Cat.1** powder

The thermal behaviour of **COF.Cat.1** was evaluated using Differential Scanning Calorimetry (DSC) in an N_2 atmosphere, covering a temperature range from 0°C to 300°C. The analysis revealed a sharp endothermic peak at 166.4°C, corresponding to the melting point of the cationic COF, with a heat of fusion (ΔH) of 187.8 J/g. These findings suggest a semi-crystalline structure for the material. Additionally, the glass transition temperature (Tg) was not identified, likely appearing as a weak endothermic transition due to molecular relaxation. Further investigations are recommended for clarity. Beyond 250°C, the decomposition of the COF was evident.

Scanning Electron Microscopy (SEM) was utilised to study the morphology of the **COF.Cat.1** sample. The SEM use an electron beam to scan the sample with a very good resolution, down to nanometres. As can be seen in **Figure 2.4**, the COF is organised as a crystallised agglomerate, heterogeneously distributed (100 µm), and on closer look (10 and 2 µm) at the agglomerates, it can be seen that these look like sheets of layers enrolled and stacked together. This disorder may be caused by the alkyl chains and the positive charges, respectively.

[9] C. Du, X. Chen, H. Wu, Z. Pan, C. Chen, G. Zhong, C. Cai, *RSC Adv*. **2023**, *13*, 24064
[10] S. Mitra, S. Kandambeth, B. P. Biswal, A. M. Khayum, C. K. Choudhury, M. Mehta, G. Kaur, S. Banerjee, A. Prabhune, S. Verma, S. Roy, U. K. Kharul, R. Banerjee, *J. Am. Chem. Soc.* **2016**, *138*, 2828

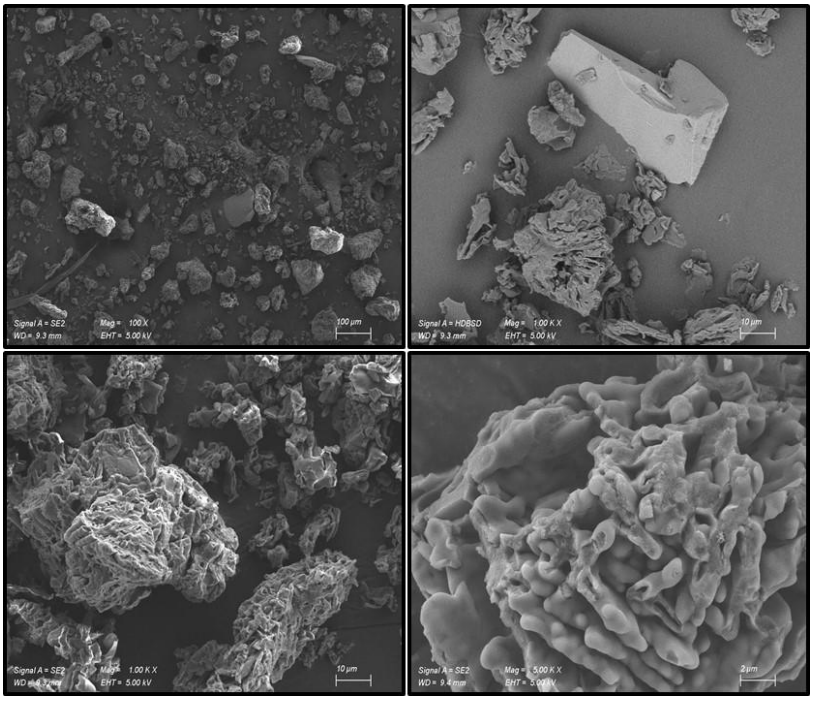

Figure 2.4: SEM images of **COF.Cat.1** sample at different scales, using a resolution of 1.5 nm at 15kV energy

2.2.3 Characterisation of the New Cationic COF.Cat.2

The IR spectra for the starting materials and three COFs: iminic, aminic, and cationic, were analysed to track structural changes (**Figure 2.5**). For **COF.2A**, a peak at 1685 cm^{-1} indicates the iminic functional group. The absence of the C=O stretching vibration peak (1697 cm^{-1}) from aldehyde **1.8**, along with the disappearance of N-H (3368 cm^{-1}, 3300 cm^{-1}) and C-H (1261 cm^{-1}) stretching vibrations, confirms the formation of iminic **COF.2A**. After reduction of the iminic COF, the IR spectra show the emergence of a 3330 cm^{-1} N-H stretch (secondary amine) and a 1250 cm^{-1} C-N stretch, indicating the formation of aminic **COF.2B**. However, some imine groups remained unaltered, as shown by the persistent 1685 cm^{-1} C=N stretch band. The alkylation of the amine groups is evidenced by the disappearance of secondary amine-related stretching vibrations.

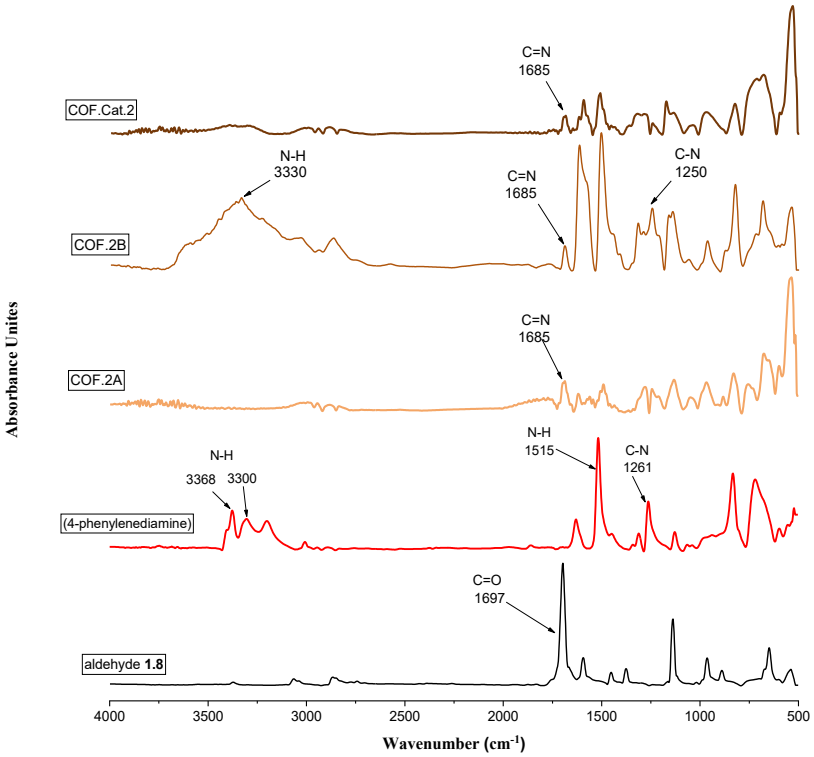

Figure 2.5: FT-IR spectra of the starting materials and the three COFs

A ^{1}H-NMR experiment to check the stability of the **COF.Cat.2** was conducted and shown in **Figure 2.6**. As can be seen in the NMR spectra, even after 48 hours at room temperature, the COF shows good stability. After 72 hours of heating at 70°C, it can be observed in the aliphatic region that the intensity of the signals has increased, and this may be due to hydrolysis or a change of the iodide counterion to hydroxyl, possibly indicated by the change in the **COF.Cat.2** colour from dark brown to orange.

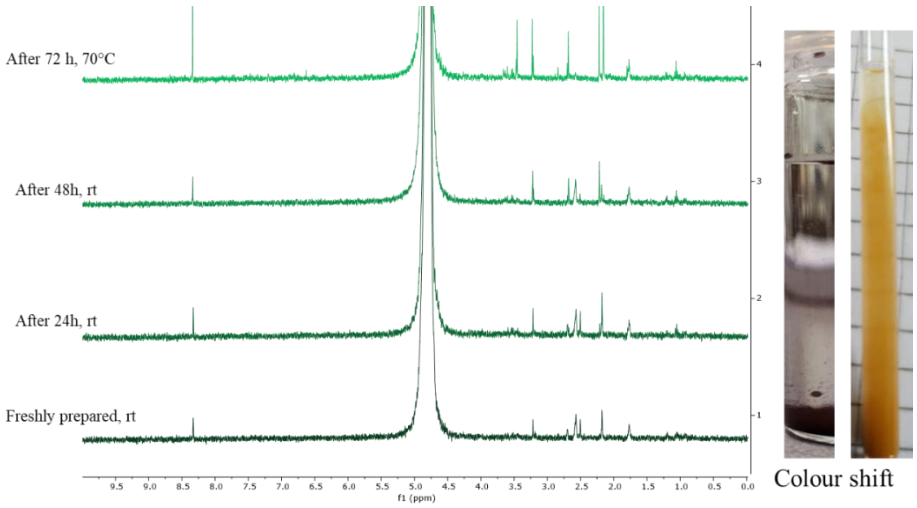

Figure 2.6. ^{1}H-NMR (600 MHz) spectra in 1M sol. NaOD/D_2O,

A thermogravimetric analysis (TGA) was performed. The resulting thermogram shows the degradation of cationic **COF.Cat.2** starts around 180°C with a steady weight loss and a maximum decomposition rate of around 400°C. Up to 400°C, the total mass loss was 21.25%. It can be seen that 7.27% of the mass consists of volatiles (> 180°C). Furthermore, Differential Scanning Calorimetry analysis was conducted for **COF.Cat.2**. The resulting thermogram shows three major peaks. The first prominent peak (102.65°C) is attributed to the evaporation process of volatiles. The other two endothermic peaks indicate the presence of two types of crystalline morphologies. Similar to **COF.Cat.1**, the glass transition temperature is not detectable.

2.3 Conclusions

Two new Cationic Covalent Organic Frameworks have been synthesised and analysed using ^{1}H-NMR, FT-IR, XRD, DSC and SEM for **COF.Cat.1** and ^{1}H-NMR, FT-IR, TGA and DSC for **COF.Cat.2**.

COF.Cat.1 was obtained in solvothermal conditions from a quaternary amine synthesised previously, starting from 1,4-phenylenediamine.

COF.Cat.2 was synthesised using commercially available compounds in a heterogeneous three-step reaction. The quaternisation of the amine groups was carried out by the mechanochemical method.

Both cationic COFs were tested for stability using NMR spectroscopy and showed good stability in 1M NaOH solution at room temperature and after heating at 70°C.

COF.Cat.1 exhibited a semi-crystalline morphology, as proven by XRD, DSC, and SEM analyses. **COF.Cat.2** displayed two types of crystalline morphologies based on DSC analyses, but further investigations are required for morphological confirmation.

Chapter 3: Anion exchange membranes with potential applications in Zinc-air batteries

3.1 Introduction

Anion exchange membranes (AEMs) are considered innovative solutions for electrochemical energy conversion and storage technologies. Research interest in AEMs has grown in recent years in the areas of fuel cells, electrolysis and solid-state batteries.[11] These membranes are solid polymers containing cationic groups, such as quaternary ammonium. They are used to separate the anode from the cathode and conduct species like HO^- in alkaline fuel cells.[12] Zinc-air battery electrolytes use alkaline aqueous solutions such as KOH and NaOH due to the higher stability of zinc in alkaline media.

3.2 Results

This topic focused on synthesising and characterising several anion exchange membranes and studying their behaviour (water absorption and ion exchange capacity) for ZAB (Zinc-air batteries) applications. These membranes were obtained by using commercially available compounds in a three-step reaction.

3.2.1 Synthesis of Anion Exchange Membranes

The new three-step reaction strategy aims, in the first step, to obtain an imine-bonded structure by reacting 1,3,5-benzenetricarboxaldehyde (BTA), 1,4-phenylenediamine (BDA) and Jeffamine (D2000, 440 or D400) in a single vessel to obtain branched frameworks within the material. The inner membrane product of trialdehyde and 1,4-phenylenediamine confers rigidity, and Jeffamine acts as a precursor for membrane formation.

[11] Y.J. Wang, J. Qiao, R. Baker, J. Zhang, *Chem. Soc. Rev.* **2013**, *42*, 5768
[12] M. Mamlouk, K. Scott, *J. Power Sources*, **2012**, *211*, 140

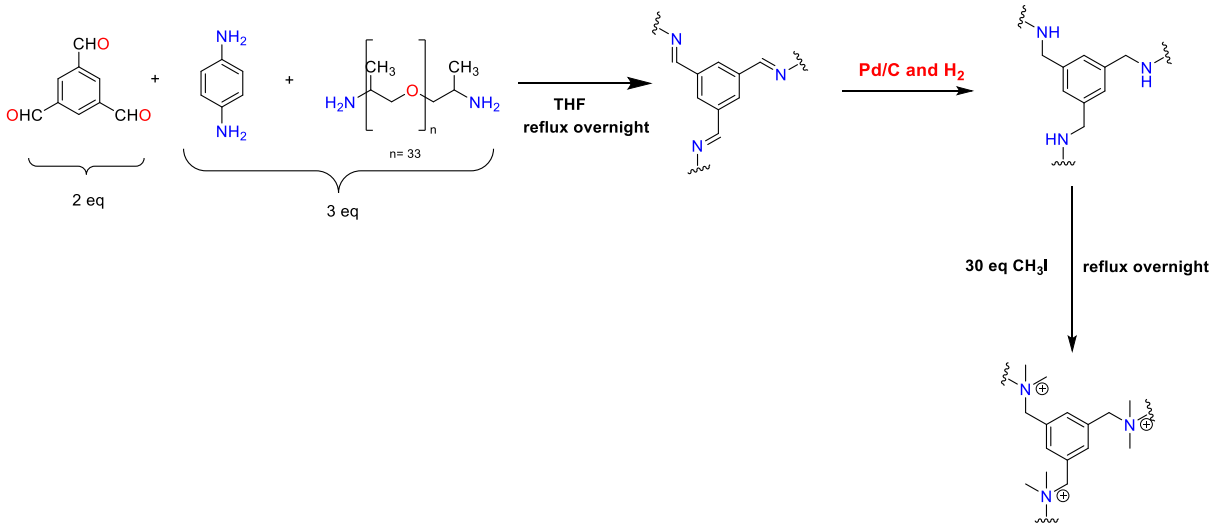

Scheme 3.0: Schematic representation of the synthetic three-step reaction strategy, which involves Pd/C and hydrogen as reducing agents

After the first step, the imine bonds were reduced with Pd/C and H_2 to amine groups, and finally, the last step consisted of quaternization of the amine groups by reaction with an excess of methyl iodide, obtaining cationic membranes (**Scheme 3.0**). Then the solutions were poured into a Teflon shape and slowly evaporated at room temperature. When the gel was formed, a thermal treatment was applied by increasing the temperature from 30ºC to 100ºC until the membrane could be removed from the Teflon shape. Water uptake was realised by introducing small parts of the membrane into distilled water and measuring the weight of the sample after 1h and 2h. Our collaborators from SINTEF Industry, Norway, have taken a different approach regarding water uptake by measuring the thickness of the membrane before and after soaking in distilled water. Using the three-step strategy explained above, membranes with different percentages of BDA (4-phenylenediamine) and Jeffamine D2000 were obtained (**Figure 3.0**). Experiments on water uptake and ion exchange capacity (EIC) were performed by our collaborators from SINTEF Industry.

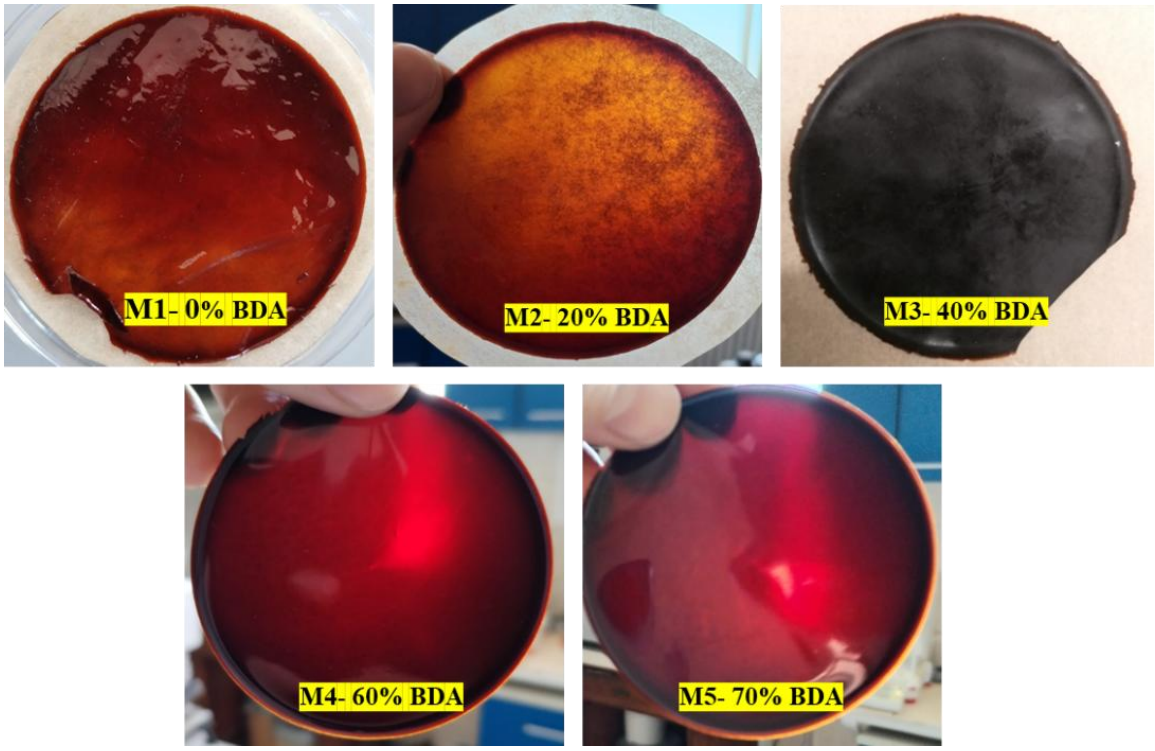

Figure 3.0: The membranes with Jeffamine D2000 containing different % of BDA

The results are shown in **Table 3.1**. Increasing the percentage of BDA and decreasing the Jeffamine D2000 did not lead to better results than expected. Only membrane **M5** (70% BDA) shows water uptake and a very small IEC (0.01), but it was not suitable for ZAB experiments.

Table 3.1: Membranes with different ratios of amines, water uptake and ion-exchange capacity

Membrane code	**% of BDA**	**% of Jeffamine D2000**	**Water uptake (µm)**		**IEC mmol /g**
			Dry	**Wet**	
M1	0	100	316 ± 3	same	0
M2	20	80	213 ± 9	same	0
M3	40	60	230 ± 2	same	0
M4	60	40	399 ± 11	same	0
M5	70	30	**315 ± 8**	**318**	**0.01**

Efforts to enhance the cross-linking and hydrophilicity of Jeffamine D2000 membranes faced multiple challenges. Initially, 20% propanolamine was introduced into the reaction mixture, improving cross-linking, but water uptake remained minimal. After two hours, the

membrane lost elasticity, was damaged, and showed poor water uptake, a behaviour mirrored in 1M KOH solution.

Alternative approaches included replacing propanolamine with histamine, which yielded an insoluble orange precipitate upon methyl iodide addition, and incorporating glycerol to decompress the polymer chains and form channels. Although the membrane was successfully moulded, after a week at 90°C, water soaking caused defects and no measurable water uptake again, consistent in 1M KOH solution.

A subsequent attempt utilised ammonium chloride as a template, leveraging NH_4^+ ions for complexation with ethylene glycols. While a minor precipitate formed after alkylation, the membrane's behaviour remained similar to the glycerol-incorporated version.

Plastic membranes were obtained using Jeffamine 440, and water uptake was not improved. The weight of the membrane didn't change even after several hours, but in a 1M KOH solution, the membrane shrunk and was destroyed, making it unsuitable for ZAB experiments.

Jeffamine D400 was another modification to improve the performance of these types of membranes. This polymeric diamine is shorter than Jeffamine D2000 and was chosen to prevent compaction of the polymeric matrix and to improve the water uptake and IEC.

Up to 70% of BDA could be incorporated when using Jeffamine D2000, but when Jeffamine D400 was used, only 10% and 20% of BDA could be incorporated. Besides BDA two different percentages of propanolamine (**Scheme 3.2**) were incorporated into the reaction and this was the best improvement so far.

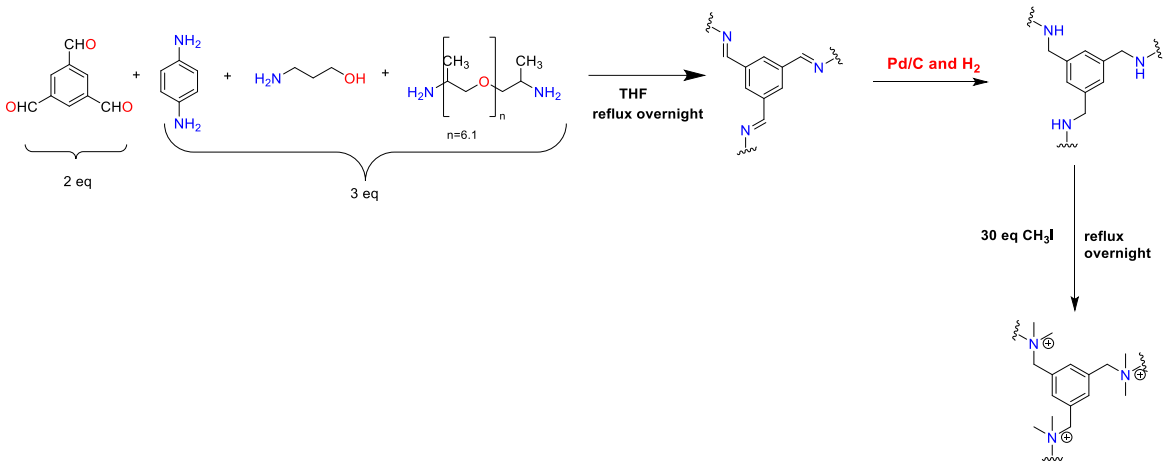

Scheme 3.2: Schematic representation of the three-step strategy using Jeffamine D400 and propanolamine

Table 3.3: Membranes with different ratios of amines, water uptake and ion-exchange capacity, using Jeffamine D400

Membrane code	% of BDA	% of propanolamine	% of Jeffamine D400	Water uptake (µm)		IEC mmol /g
				Dry	Wet	
M6	10	0	90			
M7	5	0	95			
M8	10	30	60	174 ± 8	brittle	0.25
M9	20	20	60	205 ± 34	243 ± 44	0.21

The water uptake was increased, and the best IEC was obtained, as shown in **Table 3.3**. Membrane **M8** was destroyed in contact with water, but 1M KOH solution could be processable, so a 0.25 mmol/g IEC for **M8** and 0.21 mmol/g IEC for **M9** was obtained.

3.2.2 Characterisation of Anion Exchange Membranes

The synthesis of the desired membrane was confirmed using NMR Spectroscopy (**Figure 3.1**). Samples were analysed at each reaction step. Imine formation was identified by the appearance of the signal at 8 ppm in the 1H-NMR spectrum. After reduction with Pd/C and H2, the imine signal disappeared, and a 2.5 ppm signal indicated secondary NH groups, confirming successful reduction. Finally, the disappearance of the secondary amine (NH) signal validated that alkylation was completed.

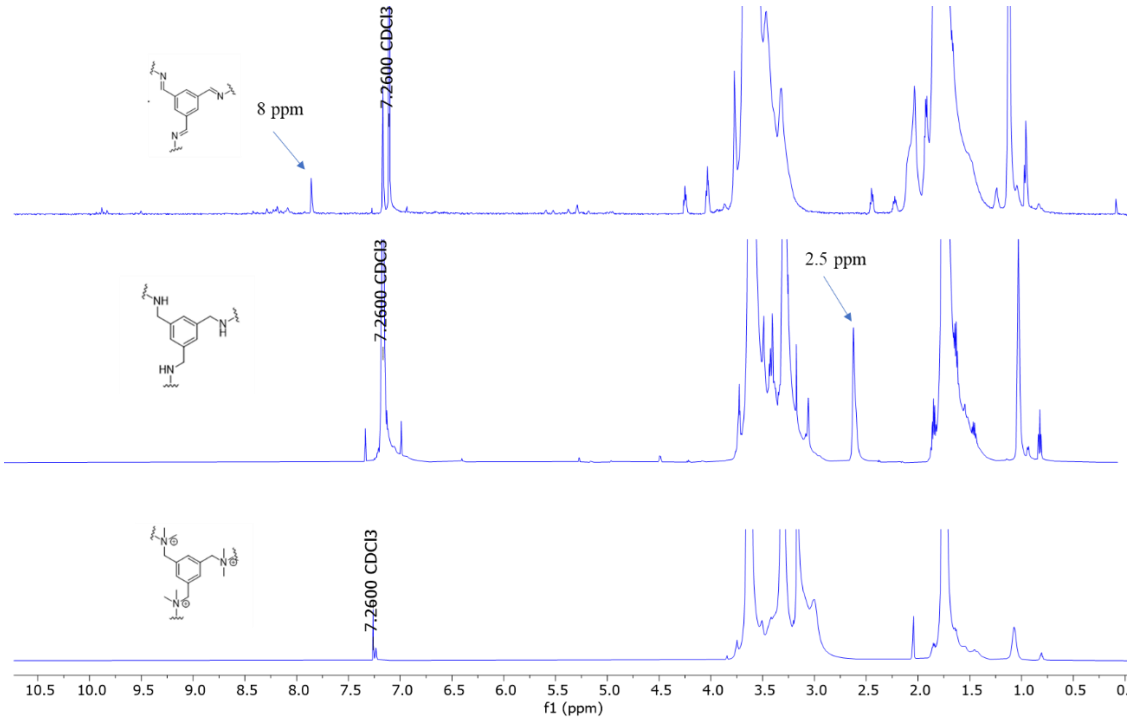

Figure 3.1: NMR spectra after each step recorded in $CDCl_3$ (400 MHz). up) after the first step; middle) after the second step, down) after the third step

The FT-IR analysis was conducted for membrane **M3** containing 40% of BDA. The analysis identifies key absorption bands in the spectrum for the Jeffamine D2000 backbone and polymeric membranes. The bands at 2970 cm^{-1} and 2930 cm^{-1} correspond to -CH_3 stretching and -CH_2- symmetric stretching vibrations, respectively. The region between 2000 and 1500 cm^{-1} reveals the remaining aldehyde groups and imine connections, with imine bonds appearing at 1646.7 cm^{-1}, and no aromatic aldehyde detected. Additional peaks include 1452 cm^{-1} for -CH_3 bending and 1090 cm^{-1} for C-O-C stretching. Thermogravimetric analysis (TGA) for membrane **M3**, revealed that the degradation of the membrane starts around 200ºC and at 300ºC a higher degradation takes place.

Differential Scanning Calorimetry (DSC) analyses were conducted between 0°C and 300°C in an N_2 atmosphere. An endothermic peak at 89.52ºC, an exothermic peak at 187.5ºC and the vitreous temperature (Tg) at -51.29ºC. appeared in the DSC thermogram.

The surface morphology and cross-section of the membranes were determined using a scanning electron microscope. The surface of the **M3** is homogeneous and dense, and in some parts of the surface, it can be observed that agglomeration of dense aggregates. The thickness is 304.8µm, and the membrane looks homogeneous and dense in the cross-

section part (**Figure 3.2**). In the case of membranes **M1**, **M2**, **M4** and **M5,** no specific changes could be identified.

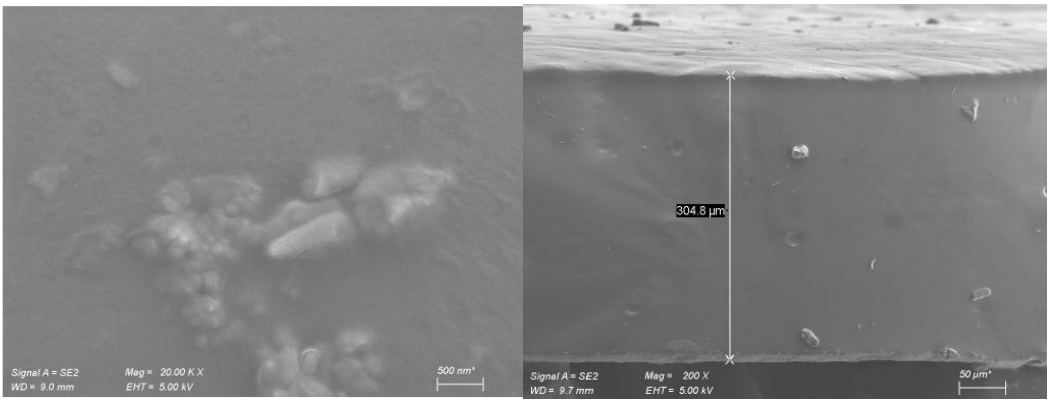

Figure 3.2: SEM images of the membrane **M3** (left) surface and (right) section

3.3 Conclusions

Nine new anion exchange membranes have been synthesised using a new three-step strategy. The membranes with Jeffamine D2000 did not exhibit water uptake and ion exchange capacity excepting membrane M5 with 70% BDA. The SEM image reveals no porosity for this kind of membrane.

The addition of propanolamine to the membrane composed of Jeffamine D2000 resulted in the membrane's degradation during the water-uptake test.

Replacing propanolamine with histamine in the membranes containing Jeffamine D2000 caused the COF to precipitate following the alkylation step.

The incorporation of glycerol and ammonium chloride into the membrane containing Jeffamine D2000 resulted in membrane degradation when water-uptake tests were performed, yielding negative results.

Replacing 1,4-phenylenediamine with aliphatic tetraethylenepentamine resulted in the formation of gels rather than membranes.

Replacing Jeffamine D2000 with branched Jeffamine 440 resulted in the development of plastic membranes that were incapable of water uptake and degraded in basic solutions.

The most favourable results were achieved with membranes containing Jeffamine D400 and propanolamine. An ion exchange capacity of 0.21 mmol/g was measured for M9 with 20% BDA, while M8 with 10% BDA exhibited an ion exchange capacity of 0.25 mmol/g.

Chapter 4: *Contributions to Carbon Dots Materials in Photovoltaics*

4.1 Introduction

Carbon dots (CDs), also known as carbon nanodots, represent a relatively new class of carbon nanomaterials with sizes below 10 nm.[13] CDs were obtained in 2004 during the purification of single-walled carbon nanotubes[14] and then in 2006 by laser ablation of a mixture of graphite powder and cement by Ya-Ping Sun and collaborators.[15] They observed no photoluminescence after the treatment of nanoscale carbon particles with 2.6 M aqueous nitric acid solution. However, after surface passivation by attaching organic species, bright luminescent emissions were noticed. The literature data presents a variety of carbon-rich materials from which CDs can be synthesised (**Figure 4.0**).

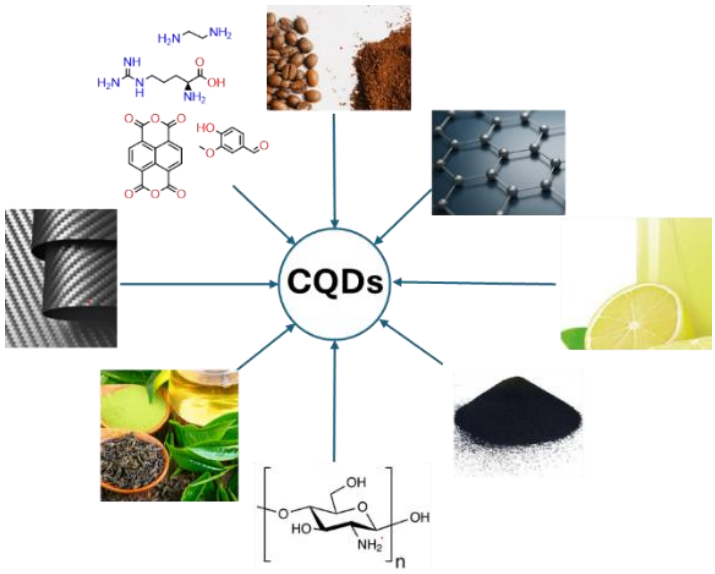

Figure 4.0: Different carbon-rich materials used for obtaining CDs

[13] Y. Wang, A. Hu, *J. Mater. Chem. C*, **2014**, *1*, 6921
[14] X. Xu, R. Ray, Y. Gu, H.J. Ploehn, L. Gearheart, K. Raker, W. A. Scrivens, *J. Am. Chem. Soc.* **2004**, *126*, 12736
[15] Y.P. Sun, B. Zhou, Y. Lin, W. Wang, K. S. Fernando, P. Pathak, M.J. Meziani, B. A. Harruff, X. Wang, H. Wang, J. *Am. Chem. Soc.* **2006**, *128*, 7756

4.2 Results and Discussions

The main objective of this work is to synthesise and describe the optical properties of carbon dots (CDs) functionalised with 1,4-phenylenediamine (**CDs-PDA**) and four different polymers: PEG1500N (**CDs-PEG**), Jeffamine D2000 (**CDs-Jeff**), NIPAM (**CDs-NIPAM**), and PNIPAM-NHS (**CDs-PNIPAM-NHS**). Other objectives are investigating the electroluminescence properties of CDs in LED devices and the use of two different types of functionalized CDs in broadband photodetector hybrids with graphene derivatives.

The first step in the synthesis is to activate the carbon surface (**Scheme 4.0**), and for this, the carbon powder was refluxed for 18h in a 2.6 M solution of HNO_3 to oxidise the surface of the material into carboxylic acid residues. The resulting mixture was dialysed against deionised water to neutral pH, and then the smallest carbon particles were extracted in the supernatant after the centrifugation of the samples (6000 rpm, 1h), followed by lyophilisation to obtain a powder.

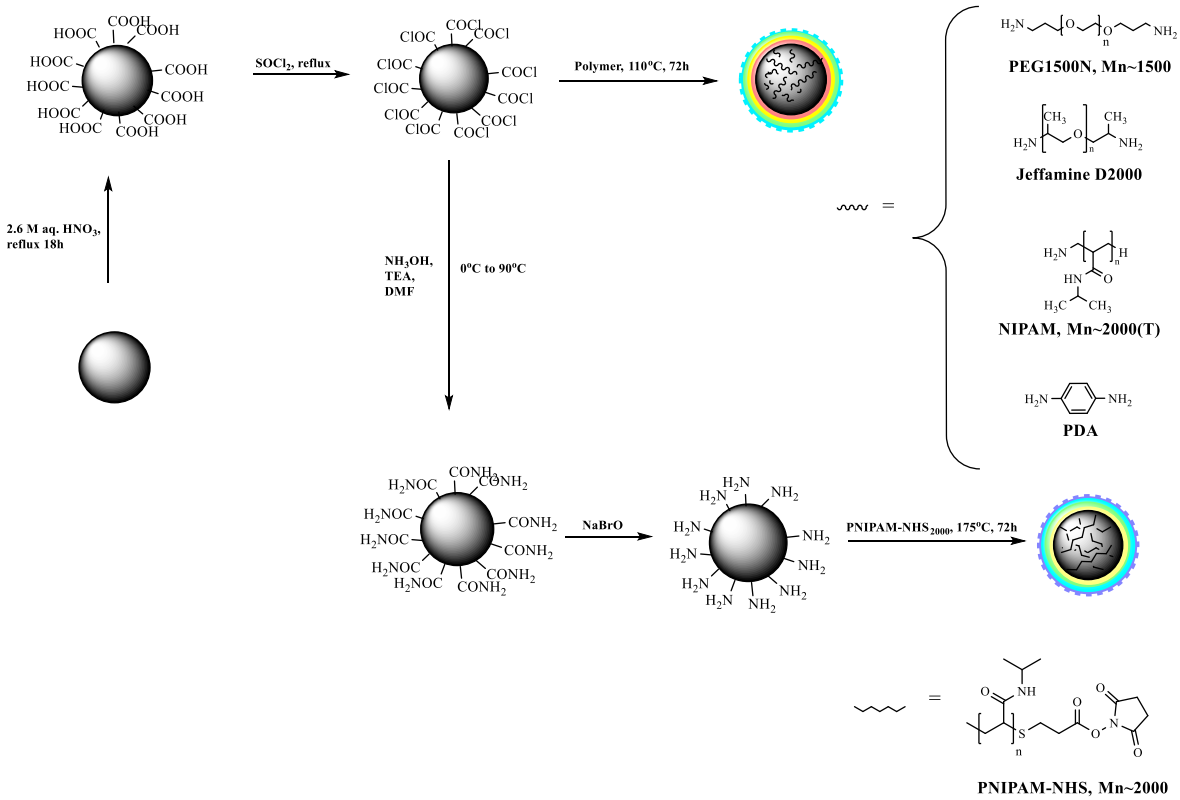

Scheme 4.0: Schematic representation of the process steps used to synthesise the passivated CDs

The second step consists of converting the carboxylic groups to acyl chlorides to increase the reactivity and favour the amidation reaction with the aromatic amine and amino-terminated polymers, by treating the oxidised nanopowder with thionyl chloride at reflux for about 17h. The last step is to functionalize with the aromatic diamine and polymers.

A particular case (with blue in **Scheme 4.0**) was the modification of the surface of the carbon nanoparticles after thionyl chloride treatment to obtain primary amine functionality, required to ensure that the NHS polymer would attach properly to the carbon dots surface. The procedure followed for this step was adapted from the literature[16] and consisted of a Hofmann degradation.

The emission spectra of CDs were recorded in an aqueous solution to investigate the luminescent properties of these materials. After these investigations, the materials exhibited similar behaviour and the major interest was in obtaining devices using CDs-PDA and CDs-NIPAM materials.

4.2.1 Morphological Properties of CDs-PDA

The nanoparticles obtained after fractionation show a crystalline structure, with a graphitic nucleus, and dimensions of about 4 nm as resulted from the recorded HRTEM images (**Figure 4.1**).

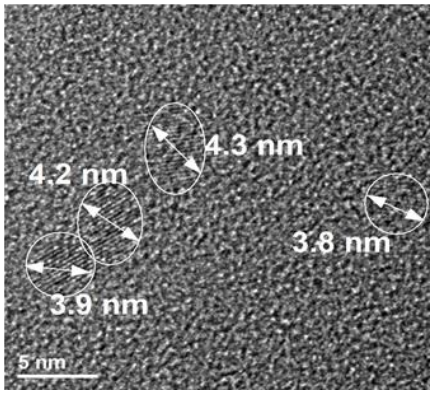

Figure 4.1: HRTEM of CDs-PDA after chromatographic separation on Sephadex^{TM} G-100 gel

[16] W. Zhang, J. Ma, D. Gao, Y. Zhou, C. Li, J. Zha, J. Zhang, *Prog. Org. Coat.* **2016**, *94*, 9

4.2.2 Photoluminescent Properties of CDs

The emission spectra of CDs-PDA F2 and F3 in aqueous solution (**Figure 4.2**) show visible-range emission. Excitation at wavelengths over 420 nm leads to diminished and red-shifted emission signals, extending beyond 570 nm. Functionalized carbon nanoparticles display weak fluorescence bands, possibly from various oligomers formed during oxidation, due to the overlap of emitting entities. Both spectra of F2 and F3 have identical shapes, but F3 exhibits the highest fluorescence quantum yield (approximately 1%).

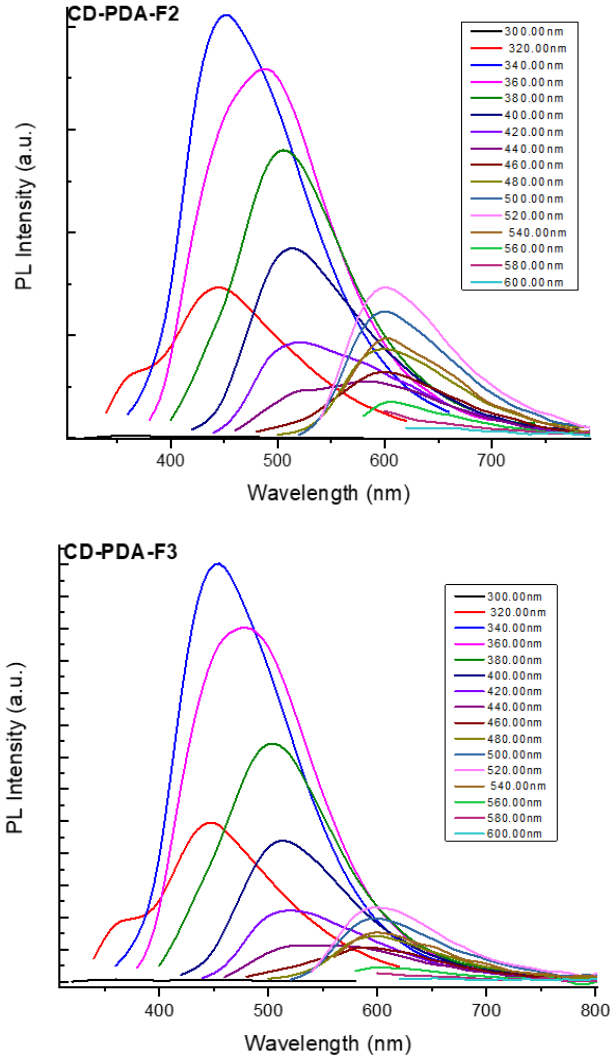

Figure 4.2: Photoluminescence spectra of CDs-PDA F2 and F3 in aqueous solution at different excitation wavelengths

The fluorescence spectra plotted in **Figure 4.3** shows that, after excitation at different wavelengths (between 250 and 600 nm, depending on the material), the fractions

show emission in the visible range, and the quantum yield is attached to each spectrum. The fluorescence quantum yield of functionalized carbon nanoparticles at different excitation wavelengths was determined and calculated using quinine sulfate as a standard. The fluorescence spectra display characteristic quantum dots behaviour, which implies that the emission maxima were progressively red-shifted, and the intensity reduced with increasing the excitation wavelength. The most fluorescent fraction of each type of material was chosen from each type of material for studying the emissive behaviour. CDs passivated with PEG1500N presented the best fluorescent quantum yields at 350 nm: 15.61% for CDs-PEG-F2, 23.77% for F3 and 13.63% for F4.

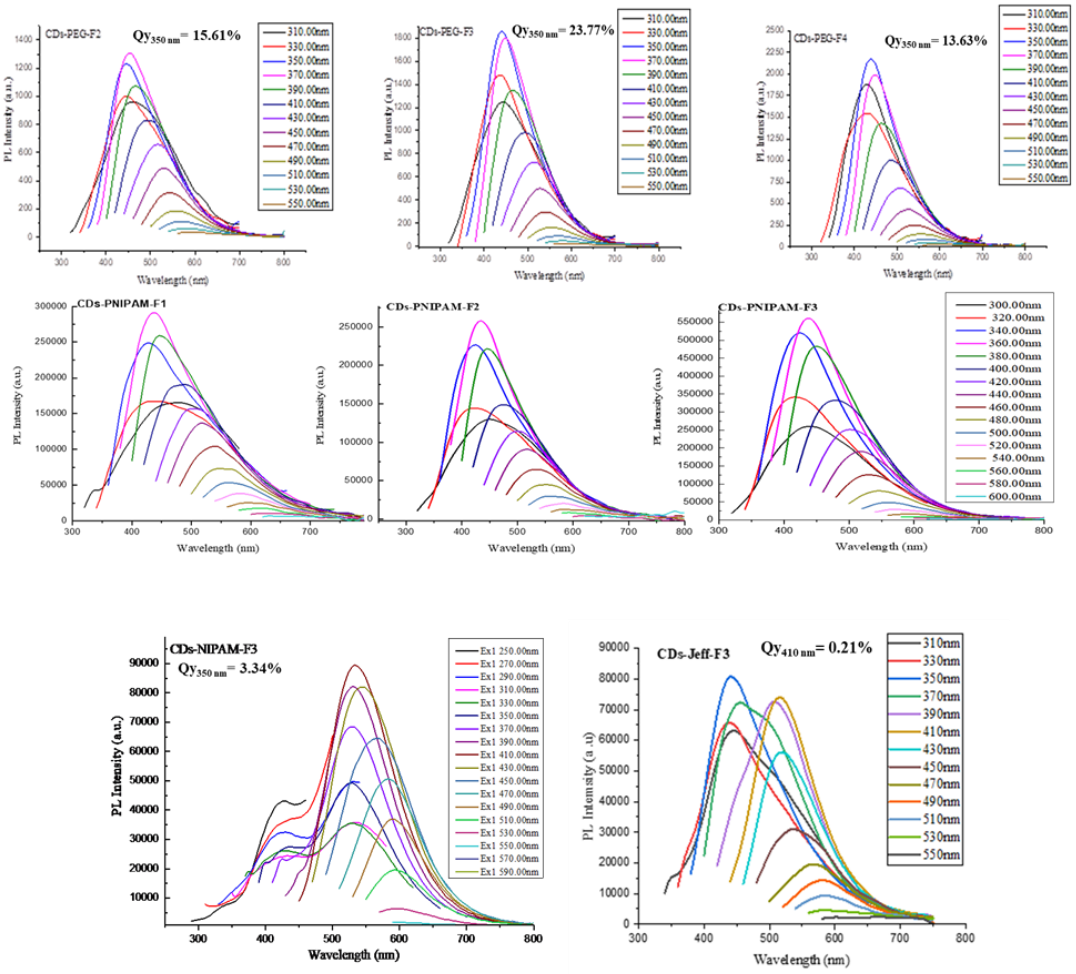

Figure 4.3: Emission spectra for different fractions of CDs passivated with PEG, PNIPAM-NHS, NIAM and $Jeff_{2000}$ and the quantum yield values for the most fluorescent fractions

4.2.3 Investigation of transport properties for CDs-PDA and CDs-NIPAM materials

Partners from IMT Bucharest utilised **CDs-PDA-F2**, **CDs-PDA-F3**, and **CDs-NIPAM-F3** to construct LED devices with a multilayer structure (ITO/PEDOT-PSS/**PolyTPD**/**CDs**/Al). The layers were deposited using spin-coating followed by aluminium cathode evaporation. PEDOT-PSS served as the hole injection layer (HIL), while PolyTPD was the hole transport layer (HTL), and CDs acted as electroluminescent material (EL). Two simplified reference LED structures, ITO/PEDOT-PSS/**PolyTPD**/Al and ITO/PEDOT-PSS/**CDs**/Al, were developed to independently assess the contributions of **PolyTPD** and **CDs**.

The ITO/PEDOT-PSS/**PolyTPD**/Al LED configuration was characterised by the absence of CDs, with and without UV-ozone treatment for the Poly-TPD at the **PolyTPD**/Al interface. For this reason, two LEDs (LED_{22} and LED_{24}) were made. It can be well observed that the UV-ozone surface treatment of the PolyTPD film at the PolyTPD/Al interface in LED_{24} leads to a significant limitation of the LED emission (**Figure 4.4**).

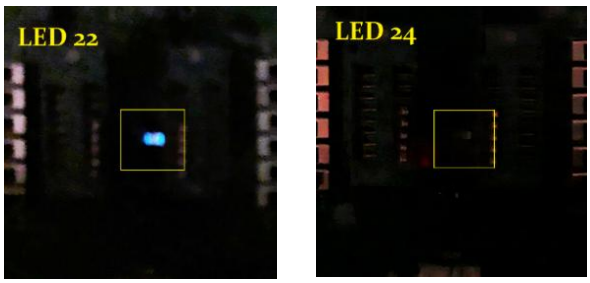

Figure 4.4: LED_{22} emission (ITO/PEDOT-PSS/**PolyTPD**/Al) and LED_{24}

The presence of CDs as active material was evaluated in an ITO/PEDOT-PSS/**CDs**/Al LED configuration structure without the hole transport layer. As a first observation, the LED structure in this configuration does not show any light emission. In the absence of the PolyTPD layer (hole transporter), the number of holes may be insufficient to generate and sustain photon emission recombination.

An ITO/PEDOT-PSS/PolyTPD/**CDs**/Al LED configuration was tested using three types of CDs as active materials: **CDs-PDA-F2**, **CDs-PDA-F3**, and **CDs-NIPAM-F3**, both with and without UV-ozone treatment. In the case of **CDs-PDA-F2**, two devices were built: LED_{19} (without UV-ozone treatment) and LED21 (with UV-ozone treatment). The UV-

ozone surface treatment caused degradation of the LED emitting surface, making LED_{19} the most effective configuration. Based on this, a 3×2 LED matrix using the LED_{19} setup was developed (**Figure 4.5**).

a.) b.) c.)

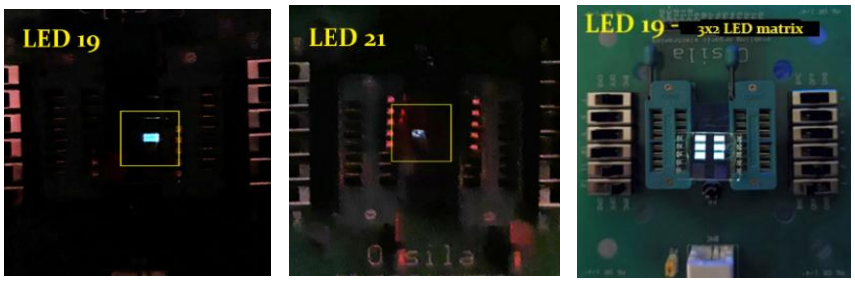

Figure 4.5: LED emissions for ITO/PEDOT-PSS/PolyTPD/**CDs-PDA-F2**/Al configuration a.) without UV-O_3 treatment, b.) with UV-O_3 treatment and c.) 3x2 LED matrix

Further investigations of the 3×2 LED matrix using the LED_{19} configuration revealed a broad electroluminescence spectrum (400–800 nm) at a constant voltage of 9V and currents of 50 mA and 100 mA. The measured Commission International de l'Eclairage (CIE) coordinates were 0.33, 0.33, which are close to the required performance for indoor portable devices (CIE 0.32, 0.34, CRI 91 at 50 mA and 9V). The electroluminescence remained stable for over 60 minutes when viewed through the transparent ITO anode.

For the **CDs-PDA-F3** active material, two LED devices (LED_{20} and LED_{23}) were fabricated using the same process as **CDs-PDA-F2** (**Figure 4.6**). Emission spectra comparisons revealed that UV-ozone surface treatment of the **PolyTPD** film at the **PolyTPD**/**CDs-PDA-F3** interface caused a reduction in LED emission intensity and a wavelength shift in the emitted light.

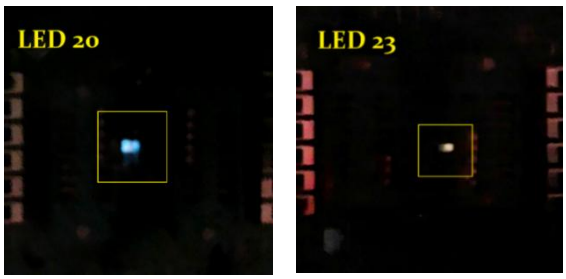

Figure 4.6: left (ITO/PEDOT-PSS/PolyTPD/ **CDs-PDA-F3**/Al configuration of LED_{20}) and right (ITO/PEDOT-PSS/PolyTPD/ **CDs-PDA-F3** (***UV-O₃***)/Al configuration of LED_{23})

Devices LED_{16} and LED_{25}, using **CDs-NIPAM-F3** as the active material, share the same configuration as earlier devices, with LED_{25} featuring UV-O_3 treatment. The UV-O_3 surface treatment resulted in slight degradation of the LED emitting surface (**Figure 4.7**). Additionally, even without UV-ozone treatment, the LED emitting surface showed uneven luminous intensity, indicating possible charge transfer non-uniformities at the PolyTPD/**CDs-NIPAM-F3** interface.

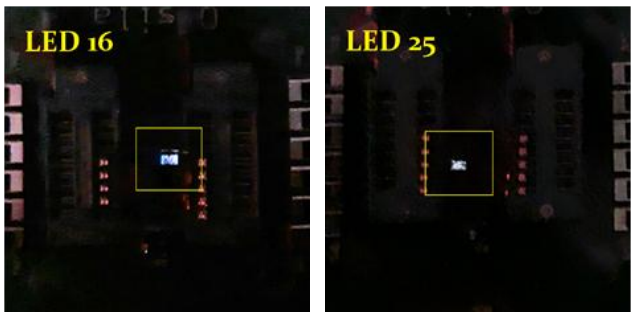

Figure 4.7: left (ITO/PEDOT-PSS/PolyTPD/**CDs-NIPAM-F3**/Al configuration for LED_{16}) and right (ITO/PEDOT-PSS/PolyTPD/**CDs-NIPAM-F3** (***UV-O_3***)/Al configuration for LED_{25})

4.2.4 CDs-graphene hybrids with broad photoresponsivity

Flexible photodetectors combining two types of carbon dots (**CDs-PEG** and **CDs-NIPAM**) with graphene-derivative hybrids were developed by IMT Bucharest. **CDs-PEG-F3** (QY ~24%, λ_{370} = 453 nm) and **CDs-NIPAM-F3** (QY ~4%, λ_{350} = 440 nm, λ_{410} = 515 nm) were combined with graphene derivatives, including reduced graphene oxide (rGO) and nitrogen-doped graphene, synthesised at INCDTIM Cluj-Napoca. These hybrids were tested on flexible polydimethylsiloxane (PDMS) substrates.

While rGO and N-doped graphene films showed negligible photoresponsivity, hybrids incorporating CDs demonstrated clear photoresponsivity: **CDs-PEG-F3**/hydrothermally N-doped GO hybrid yielded 0.02 mA/W and **CDs-NIPAM-F3**/hydrothermally N-doped GO hybrid showed a significantly higher response, reaching 0.09 mA/W at 40 mW/cm² (1V bias) and 1.25 mA/W at 70 mW/cm² (5V bias).

The hybrid films demonstrated reliable photo-switching characteristics under white light at 40 mW/cm² and low bias voltage. Key factors affecting photodetector (PD)

performance include CDs-graphene interactions, graphene oxidation/reduction levels, and doping. These PD hybrids show potential for enhancing silicon-based PD performance and could serve as a foundation for developing wearable medical devices for real-time health monitoring.

4.3 Conclusions

Five types of CDs with fluorescent properties were obtained following surface passivation with PDA and four different polymers (PEG1500N, Jeffamine D2000, NIPAM, PNIPAM-NHS).

HRTEM analysis revealed a graphitic structure approximately 4 nm in size for CDs-PDA.

The carbon nanoparticle surface's functional group modifications to the amino group needed to attach the PNIPAM-NHS polymer, were successfully achieved and proved by FT-IR analysis.

The highest quantum yield was obtained for CDs-PEG-F3 (QY350 = ~ 24 %) and the weakest for CDs-Jeff-F3 (QY410 = 0.21%).

CDs-NIPAM-F3, CDs-PDA-F2 and CDs-PDA-F3 were selected to be used as active materials for constructing light-emitting diodes. The addition of a hole transporter (PolyTPD) to the classical configuration ITO/PEDOT-PSS/CDs/Al led to emission and the best results were obtained for the LED19 structure, based on the configuration: ITO/PEDOT/PEDOT-PSS/PolyTPD/CDs-PDA-F2/Al. Spectral characteristics of the designed matrix showed that CIE and CRI values at 50 mA correspond to the commercial requirements recommendations.

Hybrids containing CDs-NIPAM-F3 combined with hydrothermally N-dopped graphene demonstrate better photoresponsivity than those containing CDs-PEG-F3. Such hybrids can be used to enhance traditional photodetectors and could be a step forward for future wearable devices such as health monitors.

Chapter 5: Access to Unsymmetrical Macrocycles for Surface Deposition

5.1 Introduction

There is a research interest in graphene interactions with different molecules to obtain catalysts for different types of chemical reactions. The functionalization of graphene is a very challenging area in order to add molecules to its surface. Graphene acts as a new class of support material due to its excellent electrical conductivity[17], chemical[18] and mechanical[19] stability, and also for its large surface area.[20] Jong-Beom Baek *et al.* reported a graphene-supported non-precious metal containing metal porphyrin and phthalocyanine with applications in oxygen reduction reactions in fuel cells. The macrocycles were uniformly dispersed and anchored on the graphene surface due to the π-π stacking and oxygen-containing functional groups.[21] Other research papers present terpyridine complexes with different transition metals such as Fe, Co and Ru. Hector D. Abruna and collaborators reported the surface diffusion of a Co bis-terpyridine ($Co(tpy)_2$) containing a tripodal compound attached to the single-layer graphene through three pyrene moieties that act as an anchor, and scanning electrochemical microscopy was used to detect the activity and quantify the surface diffusion of the tripodal compound.[22]

5.2 Results and Discussion

This research aimed to synthesise and characterise an unsymmetric macrocycle decorated with a pyridine unit suitable for attaching to a terpyridine derivative and a tripodal anchor. The **Macro-Tpy** assembly was designed to attach to a modified graphene decorated with terpyridine groups through a metal to obtain a catalyst. The tripodal anchor

[17] K. S. Novoselov, A. K. Geim, S. V. Morozov, D. Jiang, M. I. Katsnelson, I. V. Grigorieva, S. V. Dubonos, A. A. Firsov, *Nature*, **2005**, *438*, 197
[18] C. Mattevi, G. Eda, S. Agnoli, S. Miller, K. A. Mkhoyan, O. Celik, D. Mastrogiovanni, G. Granozzi, E. Garfunkel M. Chhowalla, *Adv. Funct. Mater.,* **2009**, *19*, 2577
[19] C. Lee, X. Wei, J. W. Kysar, J. Hone, *Science*, **2008**, *321*, 385
[20] S. Zhang, H. Wang, J. Liu, C. Bao, *Matter. Lett.,* **2020**, *261*, 127098
[21] H.J. Choi, N. A. Kumar, J.B. Baek, *Nanoscale*, **2015**, *7*, 6991
[22] J. Rodríguez-López, N. L. Ritzert, J.A. Mann, C.Tan, W. R. Dichtel, H. D. Abruña, *J. Am. Chem. Soc.,* **2012**, *134*, 6224

was designed for attachment to graphene *via* π-π stacking interactions with pyrene moieties. This anchor contains a carboxylic group suitable for attaching heterocyclic compounds through an esterification reaction to obtain heterogeneous catalysts.

5.2.1 Synthesis and characterisation of unsymmetrical macrocycle

A new unsymmetrical macrocycle was synthesised using a straightforward strategy involving the preparation of two podands. The process began with desymmetrization protection of diethylene glycol's OH group, followed by the synthesis of pyridine derivative **2** (95% yield). A substitution reaction between derivative **5** and tosylate compound **2** under anhydrous conditions produced compound **6** (71% yield). After deprotection, alcohol **7** underwent tosylation, yielding compound **8** (81%). The final step involved a substitution reaction between tosylate **8** and bisphenol **9** in acetone at reflux for 48 hours, yielding the target podand **10** (47%) after chromatographic separation (**Scheme 5.1**).

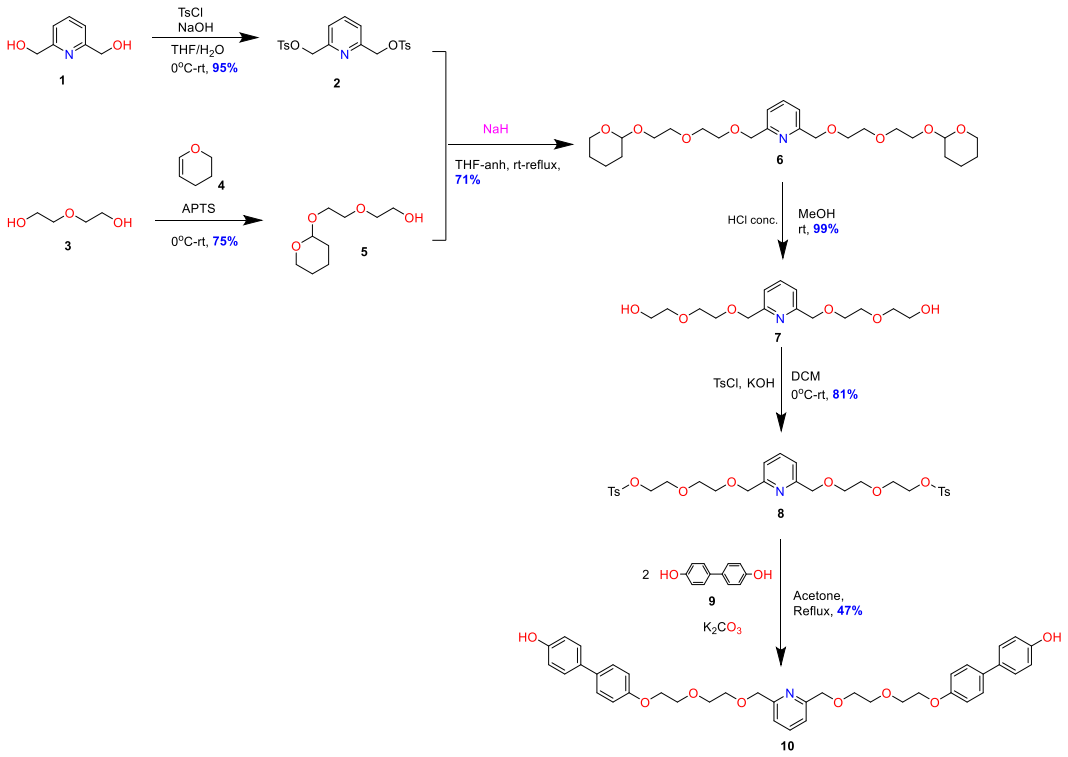

Scheme 5.1: Synthesis of target podand **10**

Podand **13** was synthesised in a single-step reaction using commercially available 5-(hydroxymethyl)benzene-1,3-diol **11** and diethylene glycol di(p-toluenesulfonate) **12**. The reaction took place in acetone under an argon stream with potassium carbonate,

followed by 24 hours of refluxing. The crude product was then purified via flash chromatography, achieving a 78% yield (**Scheme 5.2**).

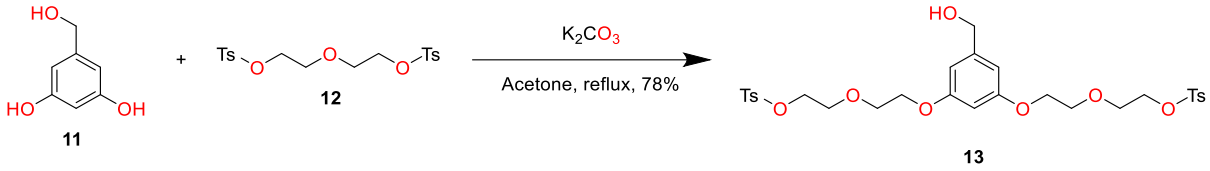

Scheme 5.2: Synthesis of target podand **13**

Podands **10** and **13** were mixed in acetonitrile for macrocyclization with caesium carbonate as the base and template, leveraging caesium's complexing ability with ethylene glycol chains. To prevent polymerisation, a high dilution was maintained. The solvent was degassed for an hour under argon, and podand **10** was added alongside dried Cs_2CO_3. After refluxing for an hour to form phenolate, podand **13** was gradually introduced at a controlled rate over 48 hours. The resulting macrocycle **14** (**Scheme 5.3**) was obtained with a 60% yield after chromatographic separation. Structural characterisation was performed using ^{1}H and ^{13}C NMR (**Figure 5.0**) and HRMS (**Figure 5.1**).

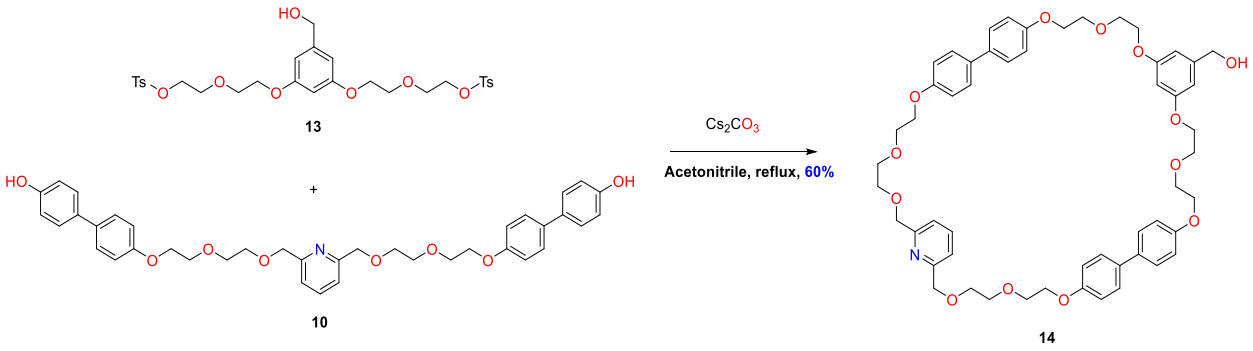

Scheme 5.3: Synthesis of target unsymmetrical macrocycle **14**

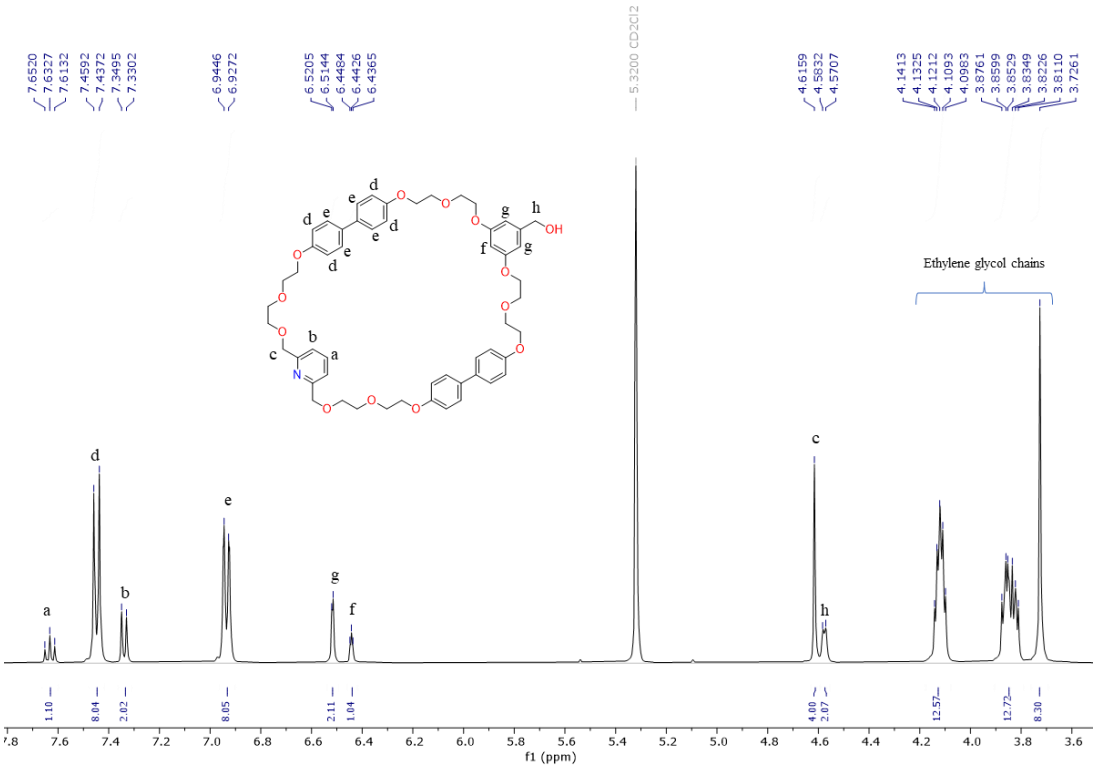

Figure 5.0: Fragment of ^{1}H-NMR (CD_2Cl_2, 400 MHz) spectra of macrocycle **14**

In the ESI(+)-HRMS spectrum (**Figure 5.1**) of macrocycle **14** it can be observed the molecular peak $[M+H]^+$ and also two more signals for complexes with Na^+ and K^+.

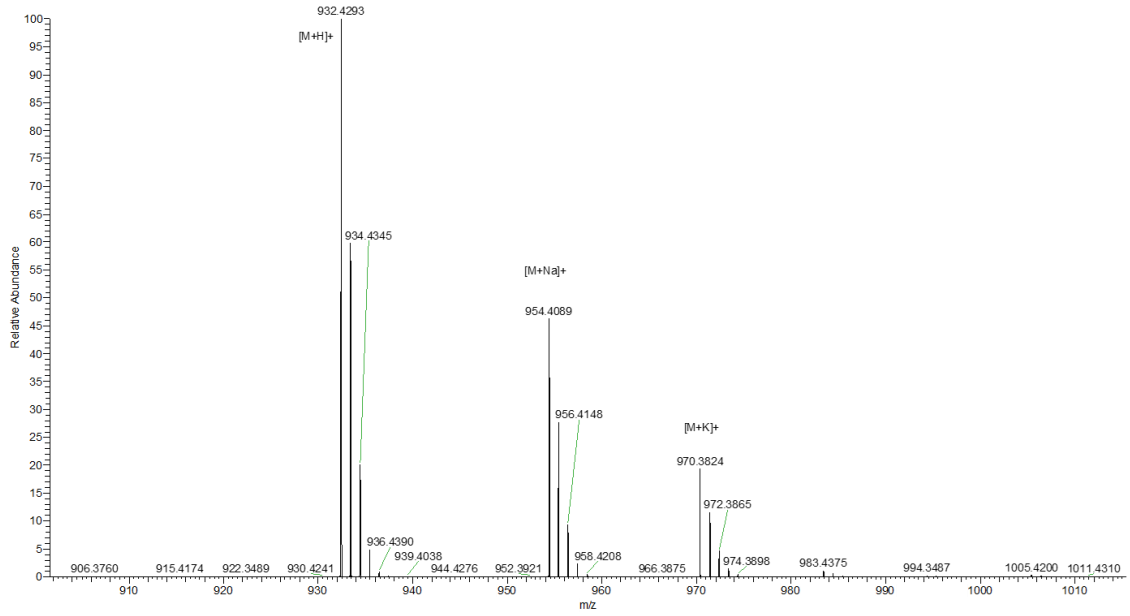

Figure 5.1: ESI(+)-HRMS spectrum of target macrocycle **14**

5.2.2 Synthesis and structural characterisation of Macro-Tpy derivative

The **Macro-Tpy** was synthesised using sodium hydride in anhydrous THF (**Scheme 5.4**). In the first step, the macrocycle alkoxide was generated, and the Tpy derivative **15** was added dropwise. After the addition of Tpy derivative **15**, the reaction was refluxed overnight. The purification consisted of simply precipitation with ethanol from a concentrated chloroform solution. **Macro-Tpy** was obtained in a 45% yield, and NMR (**Figure 5.2**) and HRMS (**Figure 5.3**) confirmed the structure.

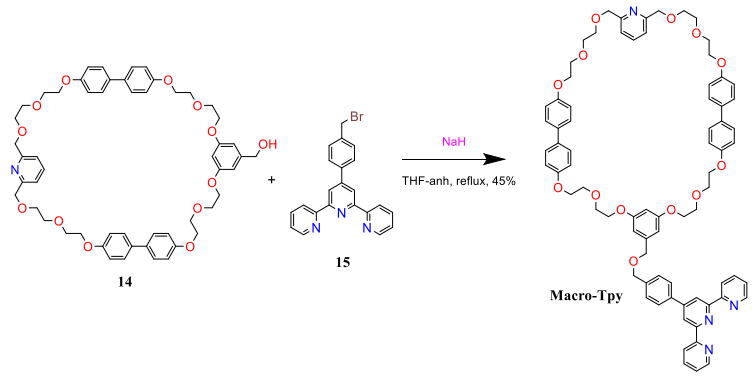

Scheme 5.4: Synthesis of target **Macro-Tpy**

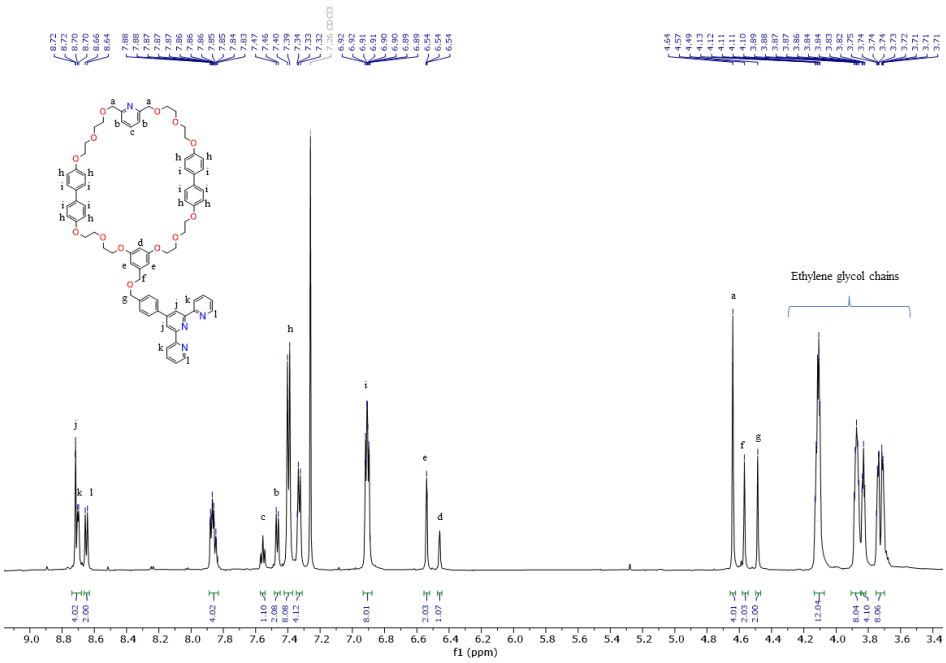

Figure 5.2: Fragment of ^{1}H-NMR ($CDCl_3$, 600 MHz) spectra of **Macro-Tpy**

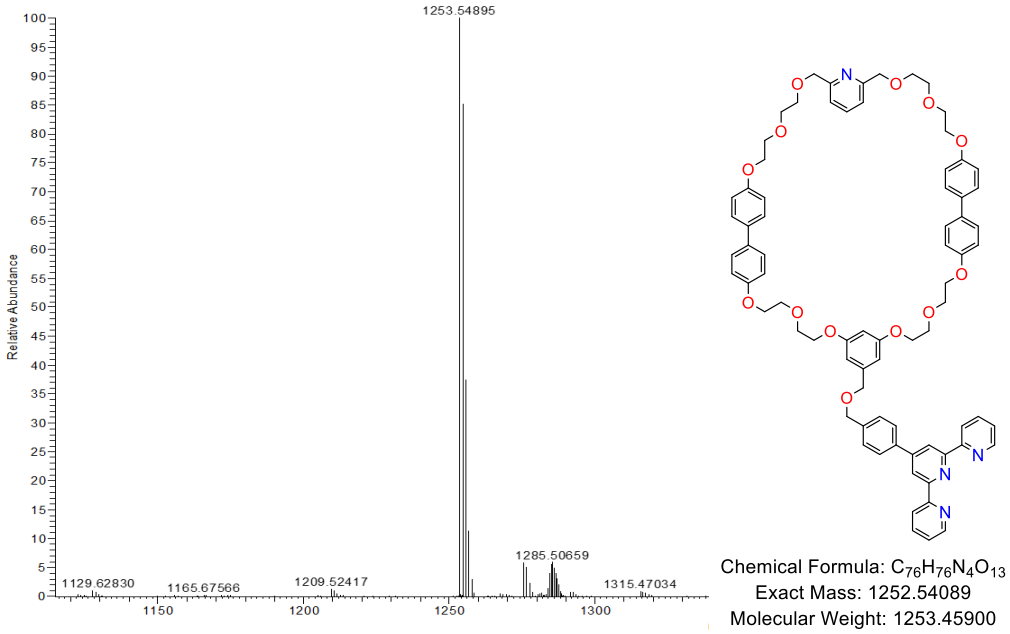

Figure 5.3: ESI(+)-HRMS spectrum of target **Macro-Tpy**

ESI(+)-HRMS spectrum (**Figure 5.3**) of **Macro-Tpy** revealed that the base peak in the spectrum is at *m/z* 1253.45895 for protonated species $[M+H]^+$.

5.2.3 Synthesis and characterisation of a tripodal anchor

The synthesis of the tripodal anchor (**Scheme 5.5**) began with the preparation of pyrene arms. Aldehyde **16** was reduced with sodium borohydride, yielding compound **17** quantitatively. The hydroxyl group was then substituted with bromine using PBr_3 in toluene at 0°C, producing compound **18** with an 80% yield. This derivative was reacted with an excess of tetraethylene glycol in anhydrous THF using NaH as the base, yielding compound **19** (55%) after chromatographic separation. Compound **20** was synthesised via tosylation in DCM at 0°C, achieving an 86% yield.

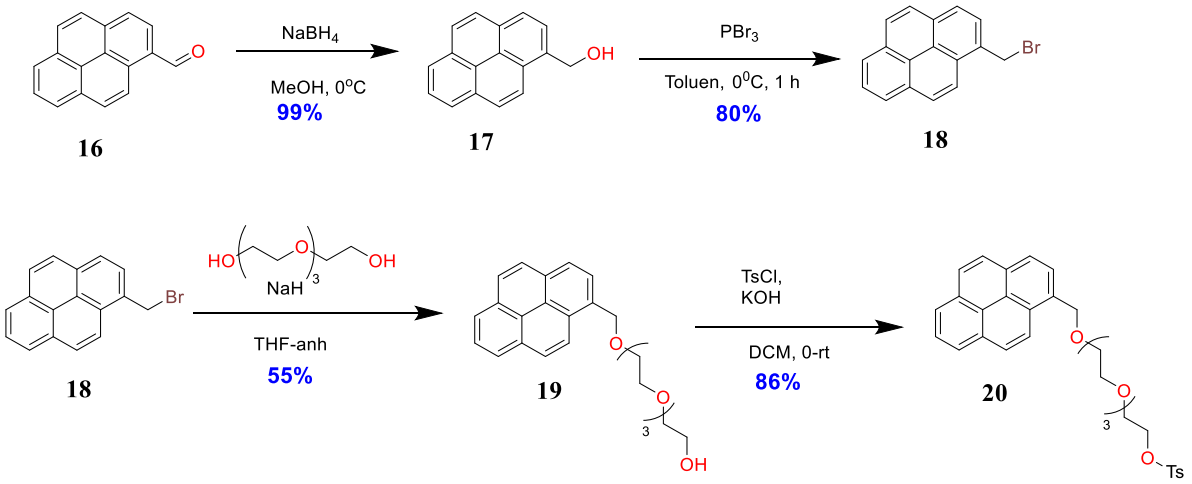

Scheme 5.5: Synthesis of pyrene derivative **20**.

Compound **29** was synthesized following a multi-step strategy. Initially, three precursor compounds were obtained based on literature methods.[23] The process began with a Grignard reaction, followed by phenol substitution using trifluoromethanesulfonic acid at 120°C for 48 hours, and hydroxyl group protection with methyl iodide, yielding excellent results. A Suzuki cross-coupling reaction with boronic acid **26** led to compound **27** (58% yield). Phenol deprotection with boron tribromide partially removed the carboxylic group, resulting in a mixture of derivatives **28** and **29**, confirmed *via* NMR. The final esterification step, using thionyl chloride in ethanol, yielded compound **29** with a high yield of 95%. Structural characterisation was completed using NMR and mass spectrometry.

[23] T. Hatano, T. Kato, *Tetrahedron*, **2008**, *64*, 8368

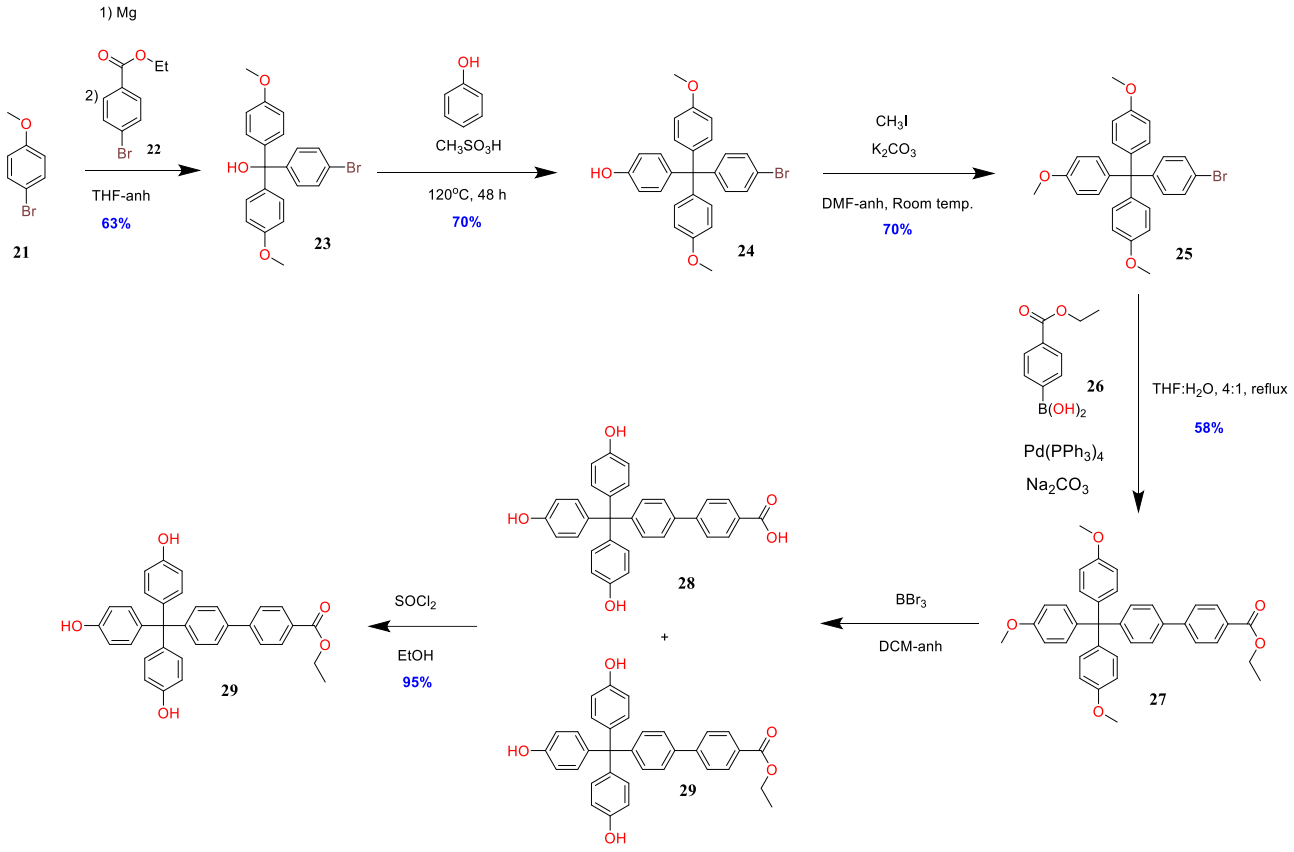

Scheme 5.6: Synthetic strategy of the target compound **29**.

The synthesis of target anchor **31** involved two final steps. First, an o-alkylation reaction between derivative **29** and pyrene derivative **20** using caesium carbonate in DMF yielded compound **30** (75%). This was followed by a saponification reaction of compound **30** with THF and a 60% NaOH solution, producing anchor **31** with a 71% yield. All compounds were purified via column chromatography and characterised using NMR (**Figure 5.4**) and mass spectrometry (**Figure 5.5**).

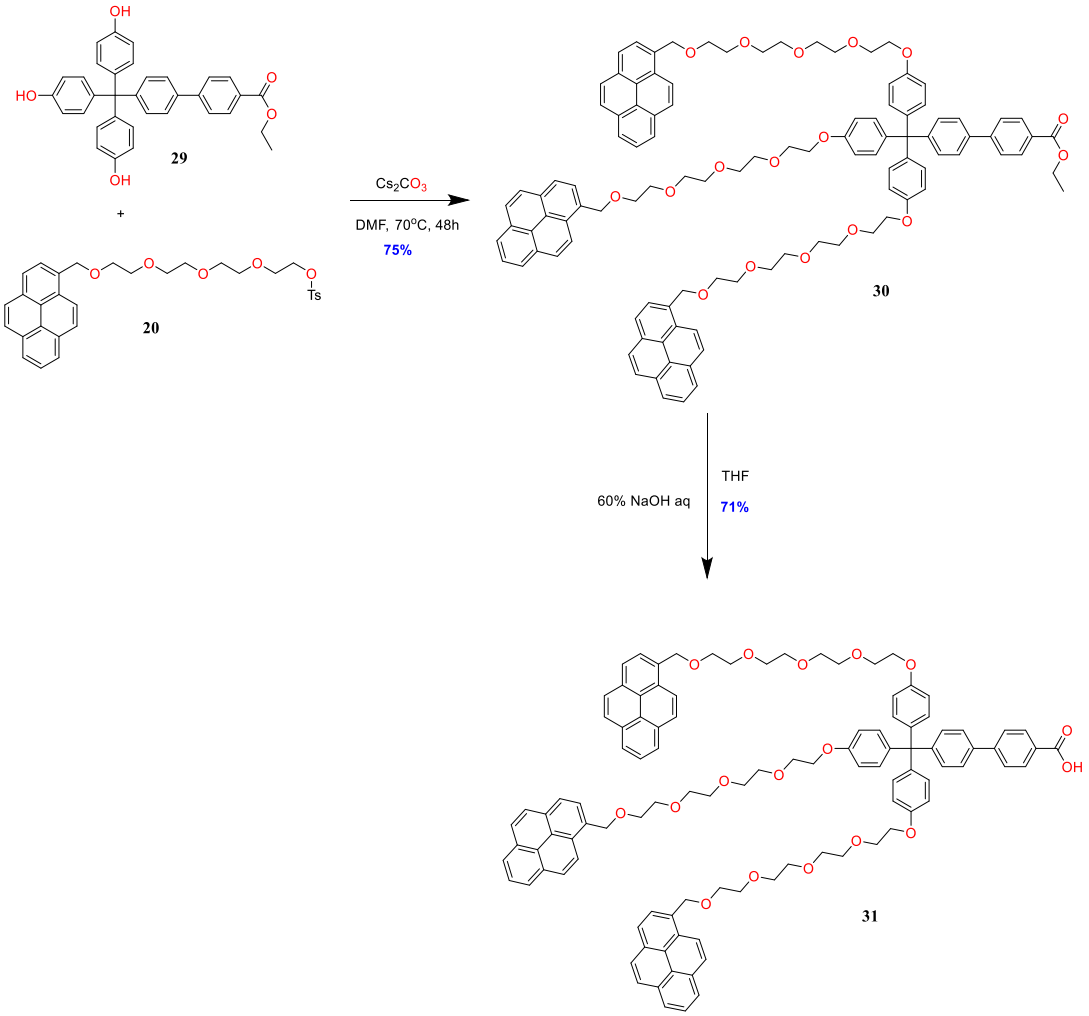

Scheme 5.7: Synthetic strategy of the target anchor **31**

The ^{1}H-NMR spectrum of anchor **31** is depicted in **Figure 5.4** and agrees with the structure of the compound. As can be seen, there are specific overlapped signals for the pyrene moiety between 7.9 - 8.5 ppm in the aromatic region and the tetraethylene glycol moiety in the aliphatic region between 3.5 – 4.5 ppm. A singlet is observed at 5.25 ppm and is assigned to the six hydrogens from the methylene's H_g directly bound to the pyrene moieties. In the aromatic region, a doublet signal for the six hydrogens H_a can be observed at 6.73 ppm and also for the six H_b at 7.04 ppm. Doublets at 7.21 ppm, 7.44 ppm and 7.61 ppm are assigned for H_c, H_d, and H_e from the tetraphenyl methane moiety.

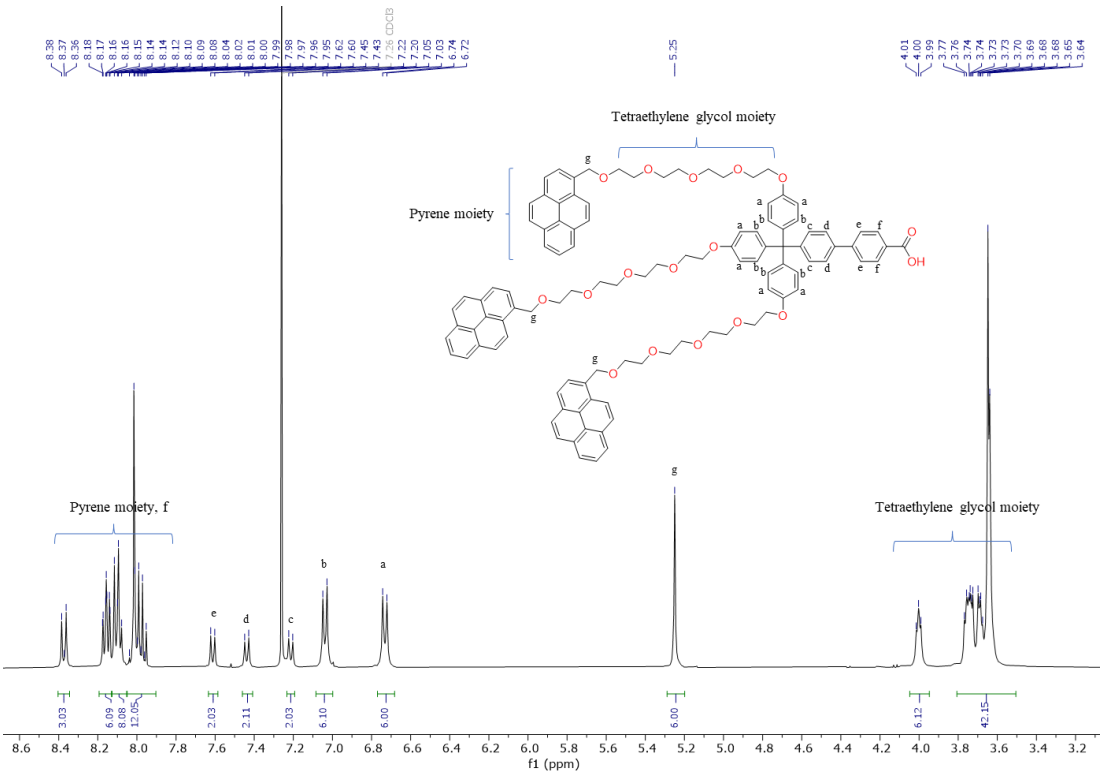

Figure 5.4: Fragment of ^{1}H-NMR ($CDCl_3$, 400 MHz) spectra of anchor **31**

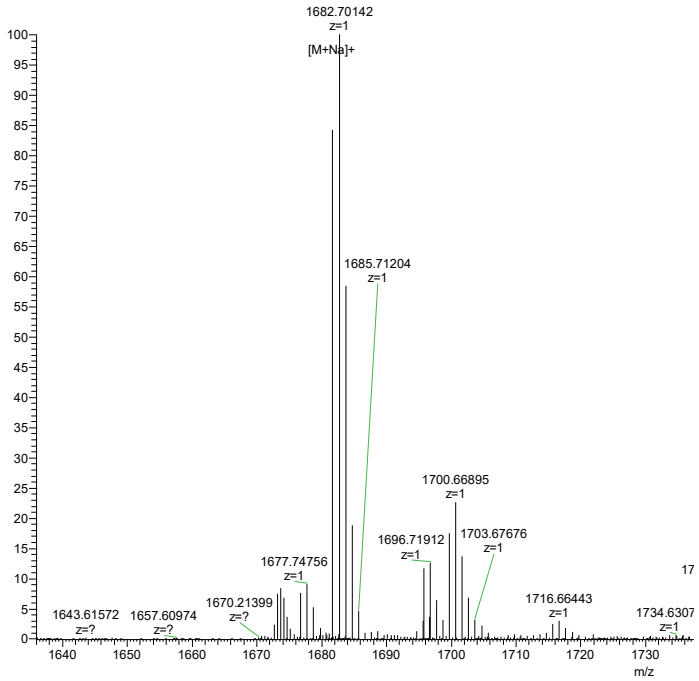

Figure 5.5: Fragment of ESI(+)-HRMS spectra of anchor **31** (*m/z* 1682.70142 for the $[M+Na]^+$ species)

5.3 Conclusions

A new unsymmetric macrocycle was obtained and fully analysed by NMR, mass spectrometry and UV-vis.

Macro-Tpy assembly was synthesised and analysed using NMR, mass spectrometry, and UV-vis. The complex **(Macro-Tpy)$_2$Fe^{2+}** obtained shows the specific band at 569 nm in the UV-vis spectrum, attributed to the formation of Fe^{2+} complexes with terpyridines.

A multi-step strategy was processed successfully, yielding the tripodal anchor **31**. ^{1}H-NMR spectrum confirmed the structure and HRMS ESI(+) provided molecular mass confirmation with the base peak for [M+Na]+ species.

General Conclusions

The thesis entitled “Development of Smart Materials for Homojunction Organic Solar Cells, Electrode Materials and Photoluminescent Carbon Dots ” is structured into five chapters concerning new: a) materials for Homojunction Organic Solar Cells; b) cationic Covalent Organic Frameworks; c) anion exchange membranes; d) electroluminescent carbon dots; e) unsymmetric macrocycle and tripodal anchor for graphene deposition.

The first chapter examines the absorption, electrochemical, and photovoltaic characteristics of a series of eight newly synthesised D-π-A compounds. These molecules incorporate triarylamine and its derivatives as electron-donating units, thiophene-based structures as π-conjugated spacers, and 2-(3-oxo-2,3-dihydro-1H-inden-1-ylidene-1-ylidene) malononitrile as the electron-accepting moiety. Their potential applications were explored in homojunction organic solar cells, adaptable to both direct and inverted configurations.

The second chapter details the synthesis of two novel Cationic Covalent Organic Frameworks (COFs) for hydrogels with potential applications in Zinc-air batteries. These cationic COFs, designed to exhibit stability in alkaline conditions, were characterised using techniques such as FT-IR, TGA, DSC, XRD, and SEM.

The third chapter details the synthesis and characterisation of nine newly developed anion exchange membranes intended for application in Zinc-air batteries. The synthesis process follows a three-step reaction initiated from commercially available precursors. Experimental findings demonstrate that strategic modifications of the reactants resulted in improved membrane properties. FT-IR, DSC, TGA, and SEM techniques have been used for characterisation.

In the fourth chapter five types of carbon dots materials were obtained by simple passivation of carbon nanopowder surface with 1,4-phenylenediamine and four polymers: Poly(ethylene glycol) bis(3-aminopropyl) amine terminated (PEG1500N), Poly(propylene glycol) bis(2-aminopropyl ether) (Jeffamine D2000), Poly(N-isopropyl acrylamide) amine terminated (NIPAM2000), and (Poly(N-isopropyl acrylamide) N-hydroxysuccinimide ester terminated (PNIPAM-NHS2000). The electroluminescence properties of the carbon dots passivated with PDA and NIPAM were investigated in a multilayer light-emitting diode

that use carbon dots as the active layer. Carbon dots passivated with NIPAM and PEG were used in combination with N-doped graphene oxide to obtain flexible photodetectors with potential applications in medical devices for real-time health monitoring.

The final chapter presents the synthesis of a novel unsymmetrical macrocycle designed for attaching to a terpyridine derivative and a tripodal anchor. The synthetic approach for the Macro-Tpy ensemble and tripodal anchor is outlined, and their molecular structures were characterised using NMR spectroscopy and mass spectrometry.